ACS OMEGA

http://pubs.acs.org/journal/acsodf

Article

Investigation of Entropy Production with Thermal Analysis under Soret and Dufour Effects in MHD Flow between Convergent and Divergent Channels

Sohail Rehman, Hashim,* Siwar Ben Hadj Hassine, Elsayed Tag Eldin, and Syed Omer Shah

Cite This: *ACS Omega* 2023, 8, 9121−9136

Read Online

ACCESS | Metrics & More | Article Recommendations

ABSTRACT: Hydromagnetic flow and heat transport have sustainable importance in conventional system design along with high-performance thermal equipment and geothermal energy structures. The current computational study investigates the energy transport and entropy production due to the pressure-driven flow of non-Newtonian fluid filled inside the wedge-shaped channel. The nonlinear radiation flux and uniform magnetic field are incorporated into the flow analysis. To be more precise, non-Newtonian fluid initiates from an inlet with the bound of the parabolic profile and leaves at outlet of a convergent/divergent channel. We assume that the channel flow is adiabatic and influenced by the wall friction. The leading flow equations are modeled via the Carreau fluid model using fundamental conservation laws. The thermodynamical aspect of the system is visualized using a two-phase model and analyses of the entropy equation due to fluid friction, ohmic heating, and diffusion of heat and mass fluxes. The modeled system of equations is normalized using a dimensionless variable mechanism. The system was elevated for the significant variation of controlling parameters. The outcomes obtained from the computational investigation are validated with the theoretical results that are available in the literature. An increasing semivertex angle and Reynolds number increase the converging channel flow. In the core flow zone, an increase in the divergent semiangle causes the flow to decelerate, while near and at the channel wall it causes a slight acceleration. Outcomes designate that the main contribution to the irreversibility is due to ohmic loss, frictional loss, and heat loss. The thermal performance and entropy production is dominant for a diverging flow. The outcomes of this research will assist in comprehending the process of entropy minimization in conjunction with the flow of nanomaterials in a nonuniform channel, which is essential in engineering processes such as the creation of micro machines, supersonic Jets, nozzles, and clean energy.

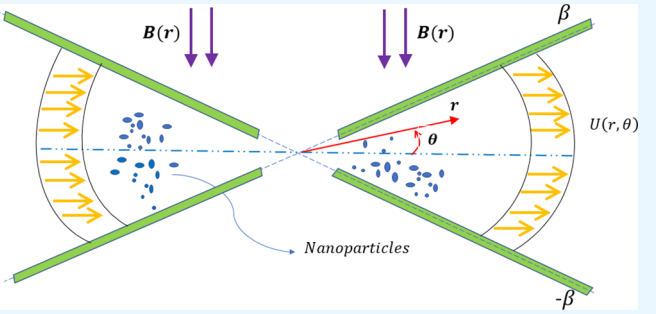

1. INTRODUCTION

In thermodynamics, the energy that is dissipated by friction, diffusion, viscous forces, and other internal resistance forces is referred to as entropy generation. Over the past few years, various researchers have created various applications to improve the entropy creation within thermodynamic processes. The significance of entropy generation in a nanofluidic system has increased because of its applicability in the disciplines of engineering and industry as well as in newly developing scientific fields. As the inaccessibility of a system's thermal energy needed for mechanical systems, entropy symbolizes the degree of unpredictability. Due to its numerous applications, including heat transfer, mass diffusion, chemical reaction, and friction, the second law of thermodynamics for entropy generation provides a direction to pledge optimal results in these infrastructures based on problems. Better estimates of entropy generation have attracted excessive attention from the research community. To establish the degree of uncertainty (irreversibility) in the performance of advanced engineering systems, Bejan[1] initiated the consideration of the entropy optimization problem. Therefore, to improve the system's functionality or output, the entropy production improved by reducing important system parameters. The laws of thermodynamics guided the development of various extrusion techniques and engineered systems. According to the first thermodynamics theory, energy is transmitted throughout a system and to its medium without any loss. The justification of energy creation is the primary shortcoming that the first thermodynamics law predicted. Mehryan et al.[2] investigated

Received: September 13, 2022
Accepted: February 2, 2023
Published: March 5, 2023

https://doi.org/10.1021/acsomega.2c05937
ACS Omega 2023, 8, 9121−9136

the entropy behavior of a magnetic third-degree fluid flow across a linearly corrugated plate and discovered that the mean Brinkman number encourages the creation of total entropy. The second law of thermodynamics is a more prominent feature when matched with first law. The second law provides the scientific tools and entropy generation to moderate the resistance. Following the second law of thermodynamics, the phenomena of entropy generation is thoroughly explored. In an L-shaped, orientated enclosure with nanoparticle flow, Seyyedi et al.[3] investigated the mechanism of entropy formation. The optimal analysis for the flow of viscoelastic nanoparticles in annuli with flexible walls was observed by Riaz et al.[4] The effects of velocity slip for optimum flow susceptible to metallic channel were documented by Turkyilmazoglu.[5] The entropy production pattern for Casson nanofluid flow caused by stretched disks was established by Khan et al.[6] The numerical entropy generation evaluation for the Crosser model was published by Hayat et al.[7]

The Jaffrey−Hamel flow in diverging/converging channels constitutes a significant class of viscous fluid. Fundamental nozzle technology in fuel sciences, converging ducts in supersonic propulsion systems, and diffusers for rockets are a few important examples. In addition, these channels offer a wide range of prospects for self-similar nonlinear boundary value problems, which can be resolved using a range of numerical and analytical techniques. By simplifying the Navier−Stokes equations, Jeffery[8] and Hamel[9] established the foundation for the study of such flows over a century ago. They investigated thermal performance in a Newtonian fluid with nonparallel walls, which is documented today as Jeffery−Hamel flow. Nagler[10] addressed the Jeffery−Hamel problem for nanofluids with nonlinear viscosity and wall friction; however he did not take into account Brownian motion or thermophoretic effects. Makinde[11] looked into the problem of fundamental irreversibility in the flow of a fluid with variable viscosity in a channel with parallel walls and nonuniform temperatures. The inherent irreversibility in a nonuniform (convergent/divergent) channel was examined by Bég and Makinde.[12] Shukla et al.[13] provided numerical simulations for the entropy minimization of the hybrid nanofluid with a slip mechanism to the Jaffrey−Hamel flow problem. Similar solutions to the Naiver−Stokes equations with entropy production in the Jaffrey−Hamel flow are provided by Weigand and Birkefeld.[14] Few more investigations considering entropy optimization and converging/diverging channels can be found in refs 15−19.

The thermodiffusion mechanism is a phenomenon in which particles are transported using several variables that are combined and calculated using a temperature gradient. When a significant density difference persists in the flow regime, the Dufour and Soret consequences take place. The relationship between driving potentials and fluxes is more complex when heat and mass conduction happen instantly in liquid motion. This manifestation occurs because of a continuous divergence in the concentration of one species in a chemical process compared to others. The combined heat and mass transfer in binary systems for transitional atomic weight gases can be facilitated by the Dufour and Soret effects. Additionally, practical and theoretical research for notable applications in energy storage units, geothermal systems, nuclear waste repositories, heat insulation, catalytic reactors, drying technologies, etc. has prompted the investigation of solutal and thermal movement in a porous medium. A flow problem involving the effects of Soret and Dufour mechanisms on mass and energy movement was designed by Chapman and Cowling.[20] The thermodiffusion or Soret effect is a process in which the mass diffusion of a flowing fluid is accelerated by a temperature differential. Mahdy[21] investigated the effects of Soret and Dufour on the MHD flow of a viscous fluid using a wavy surface. Mahabaleshwar et al.[22] emphasize the Dufour and Soret effect in a Walters-B liquid through porous media with magnetohyrodynamic flow. Discussing double-diffusive convective viscous liquid flow in a vertical chamber, Ren and Chan[23] covered the diffusion−thermo and thermodiffusion phenomena. Hayat et al.[24] established the Soret and Dufour influences in the unsteady peristaltic flow of a Prandtl liquid with viscous dissipation. Okuyade et al.[25] discuss the time-dependent magnetohydrodynamic radiative flow of a viscous liquid with diffusion−thermo and thermodiffusion. The thermodiffusion or Soret effect is a process wherein a temperature difference drives the mass diffusion of a flowing fluid. Due to the fluid concentration gradient, the diffusion−thermo or Dufour effect is linked to the heat flux.[26,27] and.[28]

Nanofluids are becoming very important because of their improved thermal efficiency. These materials play a key role in many scientific and engineering applications. Their thermal efficiency is increased by the suspension of tiny nanoparticles in the base fluid. The concept of these advanced fluids was first suggested by Choi.[29] Currently, nanofluids are extensively used in the fields of nanotechnology, heat-related devices, nuclear reactors, cooling and heating systems, radiators, generic drug processing, boiler gas outlets, biosensors, fuel chambers, caloric controlling, space technology, and numerous other useful fields. Buongiorno[30] developed the mathematical framework for the transportation of these complex fluids. Thermophoresis diffusion and Brownian diffusion, two of the seven slip mechanisms, appear to be the primary elements of nanofluid properties. Investigations into the behavior of nanofluids have a variety of approaches. In a mixed convective hydrodynamic Jeffery nanomaterial flow caused by a stretched cylinder, Hayat et al.[31] looked at the effects of activation energy and nonlinear radiation. A non-Newtonian nanomaterial magnetohydrodynamic stagnation point flow was studied by Farooq et al.[32] They took into account the impacts of linear radiation and investigated the effects of various parameters using the homotopic technique. Additionally, Basha et al.[33] investigated wedge-shaped Carreau nanofluid flow. They observed that a wedge, a plate, and stagnation point of a flat plate all reduce the fluid temperature when the suction/injection parameter is increased. Some very interesting and novel works related to nanofluids flow and heat transport characteristics have been presented.[34−39]

The above referenced works and their abundant potential applications motivated us to conduct the current numerical investigation to examine the influence of Dufour and Soret effects on radiated steady heat generated Carreau fluid transport due to pressure-driven flow in a convergent/divergent channel, as this problem has not being discussed in the literature yet. The Dufour and Soret effects are induced by the heat flux generated by a concentration gradient, and they are a key factor in the issues associated with the movement of contaminants in groundwater and the use of geothermal reservoirs. Other important industrial uses include cooling towers, sorption at an interface (adsorption) or in a bulk, drying and humidifying, segregation and doping in materials, vaporization and condensation in a mixture, boiling at a solid

https://doi.org/10.1021/acsomega.2c05937
ACS Omega 2023, 8, 9121−9136

surface, combustion, and most other chemical reactions (absorption). The importance of flow through nonparallel surfaces is demonstrated in many technology contexts. For instance, in polymer manufacturing setups, flows via nozzles, reducers, and diffusers are utilized. Molten polymer flow is successfully induced in a porous medium by flow in a nonparallel channel.

In this theoretical work, an irreversibility analysis constructed on a new multiscale together model is conducted for the first time to precisely compute the heat transference irreversibility, the mass transfer irreversibility, and the ohmic loss irreversibility of the Jaffrey−Hamel flow of a non-Newtonian liquid. The literature survey and the authors' best knowledge indicate that thus far no research has been done to date on the flow analysis and entropy production of a non-Newtonian liquid in v-shaped intersecting plates. Due to the influx for energy in everyday phenomena, developments in energy transportation and thermal transportation have attracted the interest of several engineers and researchers in a wide range of applications. The thermal transportation phenomenon dissipates a tremendous amount of energy during all thermal processes. By minimizing entropy formation in an isolated thermal system, such energy losses can be abolished or significantly minimized. The formation of entropy is significant in many domains. The entropy rate in a thermal system determines a process's likelihood and efficiency. Numerous processes, such as dissipation, mass transfer, chemical reaction, heat transfer, diffusion, molecular vibration, porous media, and electrical conduction, can result in entropy analysis. Entropy generation minimization is utilized in microchannels, chillers, reactors, and curved pipes to increase the efficiency of the equipment.

The following is a summary of the key driving factors for carrying out the current research:

- Present the analysis of heat, mass transportation, and entropy production in a Carreau nanofluid flow between intersecting plates.
- Physical descriptions of nonlinear radiant heat in addition to viscous dissipation and Ohmic heating.
- Soret and Dufour effects.
- Nanoparticle migration and thermophoresis effects.
- Entropy production and irreversibility analysis using the Bejan number.

Therefore, a mathematical model is essentially developed to illustrate the novel multiphysics of the magnetohydrodynamic interaction of a thermally radiated fluid flow in an inclined enclosure under magnetic forces. Furthermore, frictional wall conditions are implemented to analyze the flow domain. Therefore, a novel heat line and mass line model is established because the traditional methods of isotherm and isoconcentration contour visualization do not furnish the details of amplification and directional transitions of thermal and solutal fluxes. Here, the coupled nonlinear partial differential equation system governing the momentum, energy, and concentration profiles of such a converging channel flow of a non-Newtonian liquid are constructed. Later, the Keller box framework is implemented to compute the mathematical models for the heat line, mass line, and entropy generation components. Additionally, thorough numerical simulations are run for a variety of dimensionless factors related to the topic.

2. FORMULATION OF THE MODEL

Figure 1 exhibits the two-dimensional flow of a Carreau liquid between two intersecting plates, which are infinitely long in the

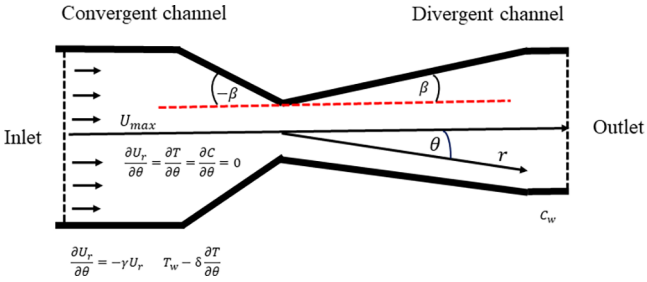

Figure 1. Schematic of two different channels with diametrically opposite inlets and outlets.

z-direction. The flow originates from a source located at an inlet between an intersection of two plates. Assume that the walls are separated at an angle 2α. We suppose that the flow drift is in the radial direction. Furthermore, the wall of the channel is lubricated, which significantly affects the velocity of the fluid in both the convergent channel ($\beta < 0$) and the divergent channel ($\beta > 0$). For the mathematical formulation of the problem, we assume that the flow is steady, incompressible, and laminar. Suppose that there is an external magnetic field B_0 applied perpendicular to the flow field, which greatly influences in fluid movement. Since the flow stream is the radial direction and depends upon r and θ, therefore $V = U_r$, $U_\theta = 0$, and $U_z = 0$. The temperature and concentration within the channel are assumed to be T and C, and those at the walls of the channel are assumed to be T_w and C_w, respectively. The energy equation is modeled using the modified Buongiorno nanofluid model, dissipation, Ohmic heating, thermal radiation and Dufour effects. We have amalgamated Soret effects in the mass diffusion equation.

With all highlighted assumption the mathematical model for the physical problem can be represented in the form of following partial differential equation:[40−46]

Mass balance equation

$$\rho_f\left(\frac{\partial}{\partial r}(rU_r)\right) = 0 \tag{1}$$

Momentum balance equations

$$\frac{1}{\rho_f}\frac{\partial p}{\partial r} + U_r\frac{\partial U_r}{\partial r} = \nu_f\left[\nabla^2 - \frac{U_r}{r^2}\right]\left[1 + \Pi^2\left(2\left(\frac{\partial U_r}{\partial r}\right)^2 + \frac{1}{r^2}\left(\frac{\partial U_r}{\partial \theta}\right)^2 + \frac{2U_r^2}{r^2}\right)^{0.5(n-1)}\right] + \nu_f\Pi^2(n-1)\left[1 + \Pi^2\left(2\left(\frac{\partial U_r}{\partial r}\right)^2 + \frac{1}{r^2}\left(\frac{\partial U_r}{\partial \theta}\right)^2 + \frac{2U_r^2}{r^2}\right)^{0.5(n-3)}\left[4\left(\frac{\partial U_r}{\partial r}\right)^2\frac{\partial^2 U_r}{\partial r^2} + \frac{6}{r^2}\left(\frac{\partial U_r}{\partial r}\right)\left(\frac{\partial U_r}{\partial \theta}\right)\left(\frac{\partial^2 U_r}{\partial r \partial \theta}\right) - \frac{2}{r^2}\left(\frac{\partial U_r}{\partial r}\right)\left(\frac{\partial U_r}{\partial \theta}\right)^2 + \frac{4U_r}{r^2}\left(\frac{\partial U_r}{\partial r}\right)^2 - \frac{4U_r^2}{r^3}\frac{\partial U_r}{\partial r} + \frac{2}{r^4}\left(\frac{\partial U_r}{\partial \theta}\right)^2\frac{\partial^2 U_r}{\partial \theta^2} + \frac{4u}{r^4}\left(\frac{\partial U_r}{\partial \theta}\right)^2\right] \tag{2}$$

https://doi.org/10.1021/acsomega.2c05937
ACS Omega 2023, 8, 9121−9136

$$\frac{1}{\rho_f r}\frac{\partial p}{\partial \theta} = \frac{2\nu_f}{r^2}\left[1 + \Pi^2\left(2\left(\frac{\partial U_r}{\partial r}\right)^2 + \frac{1}{r^2}\left(\frac{\partial U_r}{\partial \theta}\right)^2 + \frac{2U_r^2}{r^2}\right)\right]^{0.5(n-1)}\left(\frac{\partial U_r}{\partial \theta}\right) + \nu_f\Pi^2\frac{(n-1)}{2r}\left[1 + \Pi^2\left(2\left(\frac{\partial U_r}{\partial r}\right)^2 + \frac{1}{r^2}\left(\frac{\partial U_r}{\partial \theta}\right)^2 + \frac{2U_r^2}{r^2}\right)\right]^{0.5(n-3)}\left[4\left(\frac{\partial U_r}{\partial r}\right)\left(\frac{\partial U_r}{\partial \theta}\right)\left(\frac{\partial^2 U_r}{\partial r^2}\right) + \frac{2}{r^2}\left(\frac{\partial U_r}{\partial \theta}\right)^2\left(\frac{\partial^2 U_r}{\partial r\partial \theta}\right) - \frac{2}{r^3}\left(\frac{\partial U_r}{\partial \theta}\right)^3 + \frac{4U_r}{r^2}\left(\frac{\partial U_r}{\partial \theta}\right)\left(\frac{\partial U_r}{\partial r}\right) - \frac{4U_r}{r^3}\left(\frac{\partial U_r}{\partial \theta}\right) + 8U_r\left(\frac{\partial U_r}{\partial r}\right)\left(\frac{\partial^2 U_r}{\partial r\partial \theta}\right) + \frac{4U_r}{r^2}\left(\frac{\partial U_r}{\partial \theta}\right)\left(\frac{\partial^2 U_r}{\partial \theta^2}\right) + \frac{8U_r^2}{r^2}\frac{\partial U_r}{\partial \theta}\right] \tag{3}$$

Energy balance equation

$$U_r\frac{\partial T}{\partial r} = \left[\frac{k_f}{(\rho c_p)_f} + \frac{16\sigma^* T_w^3}{3k^*(\rho c_p)_f}\right]\left[\frac{1}{r}\left(\frac{\partial T}{\partial r}\right) + \left(\frac{\partial^2 T}{\partial r^2}\right) + \frac{1}{r^2}\left(\frac{\partial^2 T}{\partial \theta^2}\right)\right] + \frac{(\rho c_p)_s}{(\rho c_p)_f}\left(D_B\left[\left(\frac{\partial T}{\partial r}\right)\left(\frac{\partial C}{\partial r}\right) + \frac{1}{r^2}\left(\frac{\partial T}{\partial \theta}\right)\left(\frac{\partial C}{\partial \theta}\right)\right] + \frac{D_T}{T_w}\left[\left(\frac{\partial T}{\partial r}\right)^2 + \frac{1}{r^2}\left(\frac{\partial T}{\partial \theta}\right)^2\right]\right) + \frac{\mu_0}{(\rho c_p)_f}\left[1 + \Pi^2\left(2\left(\frac{\partial U_r}{\partial r}\right)^2 + \frac{1}{r^2}\left(\frac{\partial U_r}{\partial \theta}\right)^2 + \frac{2U_r^2}{r^2}\right)\right]^{0.5(n-1)}\left[1 + \Pi^2\left(2\left(\frac{\partial U_r}{\partial r}\right)^2 + \frac{1}{r^2}\left(\frac{\partial U_r}{\partial \theta}\right)^2 + \frac{2U_r^2}{r^2}\right)\right] + \frac{\sigma B_0^2 U_r^2}{(\rho c_p)_f r^2} + \frac{K_T D_B}{C_s c_p}\left(\frac{1}{r}\left(\frac{\partial C}{\partial r}\right) + \left(\frac{\partial^2 C}{\partial r^2}\right) + \frac{1}{r^2}\left(\frac{\partial^2 C}{\partial \theta^2}\right)\right) \tag{4}$$

Concentration balance equation

$$U_r\frac{\partial C}{\partial r} = D_B\left(\frac{1}{r}\frac{\partial C}{\partial r} + \frac{\partial^2 C}{\partial r^2} + \frac{1}{r^2}\frac{\partial^2 C}{\partial \theta^2}\right) + \frac{K_T D_T}{T_w}\left(\frac{1}{r}\frac{\partial T}{\partial r} + \frac{\partial^2 T}{\partial r^2} + \frac{1}{r^2}\frac{\partial^2 T}{\partial \theta^2}\right) \tag{5}$$

Boundary Conditions. The boundary conditions for modeled eqs 1−5 are the adhesion of the fluid on frictional walls, the continuity of the fluid temperature, and the concentration at the walls.[47−50]

$$\left.\begin{aligned} \frac{\partial U_r}{\partial \theta} &= -\gamma U_r && \text{for } \theta \to \beta \\ T &= T_w - \delta\frac{\partial T}{\partial \theta} && \text{for } \theta \to \beta \\ C &= C_w && \text{for } \theta \to \beta \end{aligned}\right\} \tag{6}$$

The middle line symmetry ($\theta = 0$) is as follows:

$$\left.\begin{aligned} U_r &= U_{max} && \text{for } \theta \to 0 \\ \frac{\partial U_r}{\partial \theta} &= 0 && \text{for } \theta \to 0 \\ \frac{\partial T}{\partial \theta} &= 0 && \text{for } \theta \to 0 \\ \frac{\partial C}{\partial \theta} &= 0 && \text{for } \theta \to 0 \end{aligned}\right\} \tag{7}$$

Here, μ_0, ν_f, k_f, ρ_f, c_p, σ, σ^*, C_s k^*, D_B, D_T, and K_T, designate the dynamic viscosity, the kinematic viscosity, the thermal conductivity, the density, the heat capacitance, the electrical conductivity, the Stefan−Boltzmann constant, the concentration susceptibility, the mean absorption coefficient, the Brownian diffusion, the thermophoresis diffusion, and the thermal diffusion. Furthermore, γ is the friction coefficient and describes the fluid-relative wall's friction. The channel walls are described as plane walls for $\gamma = 0$ and are perfectly rough for $\gamma \to \infty$, while δ designates the temperature slip factor.

Furthermore, the flow rate Q over the channel cross-section is provided in integral form.

$$Q = 2\int_0^\beta rU_r\,d\theta \tag{8}$$

Here $Q > 0$ for a divergent channel and $Q < 0$ for a convergent channel.

Entropy generation equation

$$N''' = \frac{k_f}{T_w^2}\left[1 + \frac{16\sigma^* T_w^3}{3k^*(\rho c_p)}\right]\left[\left(\frac{\partial T}{\partial r}\right)^2 + \frac{1}{r^2}\left(\frac{\partial T}{\partial \theta}\right)^2\right] + \frac{\mu_0}{(\rho c_p)_f}\left[1 + \Pi^2\left(2\left(\frac{\partial U_r}{\partial r}\right)^2 + \frac{1}{r^2}\left(\frac{\partial U_r}{\partial \theta}\right)^2 + \frac{2U_r^2}{r^2}\right)\right]^{0.5(n-1)}\left[1 + \Pi^2\left(2\left(\frac{\partial U_r}{\partial r}\right)^2 + \frac{1}{r^2}\left(\frac{\partial U_r}{\partial \theta}\right)^2 + \frac{2U_r^2}{r^2}\right)\right] + \frac{R_d D_B}{C_w}\left[\left(\frac{\partial C}{\partial r}\right)^2 + \frac{1}{r^2}\left(\frac{\partial C}{\partial \theta}\right)^2\right] + \frac{R_d D_B}{T_w}\left[\frac{\partial T}{\partial r}\frac{\partial C}{\partial r} + \frac{1}{r^2}\frac{\partial T}{\partial \theta}\frac{\partial C}{\partial \theta}\right] + \frac{\sigma B_0^2 U_r^2}{T_w} \tag{9}$$

The following transformation is introduced to reduce the following boundary value problem into the dimensionless form:[48−50]

$$U_r(r,\theta) = \frac{G(\theta)}{r}, f(\xi) = \frac{G(\theta)}{f_{max}}, f_{max} = rU_{max}, \xi = \frac{\theta}{\beta}, \Theta(\xi) = \frac{T}{T_w}, \Psi(\xi) = \frac{C}{C_w} \tag{10}$$

The momentum, energy, concentration and entropy equations may be written in dimensionless form using the new variables and parameters.

https://doi.org/10.1021/acsomega.2c05937
ACS Omega 2023, 8, 9121−9136

$$(f''' + 4\beta^2 f') + \frac{2\beta \mathrm{Reff}'}{(1 + \mathrm{We}^2(4\beta^2 f^2 + f'^2))^{0.5(n-1)}} - \frac{\beta^2 M^2 f'}{(1 + \mathrm{We}^2(4\beta f^2 + f'^2))^{0.5(n-1)}} + \frac{(n-1)\mathrm{We}^2}{(1 + \mathrm{We}^2(4\beta^2 f^2 + f'^2))^{0.5(n-1)}}(1 + \mathrm{We}^2(4\beta^2 f^2 + f'^2))^{0.5(n-3)}(3f'f''^2 + 32\beta^2 ff'f'' + f'^2 f''' + 64\beta^4 f'f^2) + \frac{(n-1)(n-3)(\mathrm{We}^2)^2}{(1 + \mathrm{We}^2(4\beta^2 f^2 + f'^2))^{0.5(n-1)}}(1 + \mathrm{We}^2(4\beta^2 f^2 + f'^2))^{0.5(n-5)}(f'^3 f'^2 + 16\beta^2 ff'^3 f'' + 32\beta^4 f^3 f'f'' + 16\beta^4 f^2 f'^3 + 64\beta^6 f^4 f' - 4\beta^2 f'^5) = 0 \quad (11)$$

$$\Theta'' + \frac{\mathrm{Pr}(N_B \Theta'\Psi' + N_T \Theta'^2)}{(1+R)} + \frac{\mathrm{PrEc}}{(1+R)}[(1 + \mathrm{We}^2(4\beta^2 f^2 + f'^2))^{0.5(n-1)}](4\beta^2 f^2 + f'^2) + \frac{\beta^2 M^2 \mathrm{PrEc} f^2}{(1+R)} + \frac{\mathrm{DfPr}\Psi''}{(1+R)} = 0 \quad (12)$$

$$\Psi'' - SrSc\left(\frac{\mathrm{Pr}(N_B \Theta'\Psi' + N_T \Theta'^2)}{(1+R)} + \frac{\mathrm{PrEc}}{(1+R)}[(1 + \mathrm{We}^2(4\beta^2 f^2 + f'^2))^{0.5(n-1)}](4\beta^2 f^2 + f'^2) + \frac{\beta^2 M \mathrm{PrEc} f^2}{(1+R)} + \frac{\mathrm{DfPr}\Psi''}{(1+R)}\right) = 0 \quad (13)$$

$$S_G = \frac{r^2\beta^2 N'''}{k_f} = (1+R)\Theta'^2 + \mathrm{Br}[(1 + \mathrm{We}^2(4\beta^2 f^2 + f'^2))^{0.5(n-1)}](4\beta^2 f^2 + f'^2) + \Delta(\Psi'^2 + \Theta'\Psi') + \beta^2 \mathrm{Br} M^2 f^2 \quad (14)$$

$$\left.\begin{aligned} f(0) = 1, f'(0) = 0, f'(1) + mf(1) = 0, \\ \Theta(1) = 1 - A\Theta'(1), \Theta'(0) = 0, \\ \Psi(1) = 1, \Psi'(0) = 0 \end{aligned}\right\} \quad (15)$$

Here, We $\left(=\sqrt{\frac{\Pi^2 U_{\max}^2}{r^2\beta^2}}\right)$ is the local Weissenberg number, Re $\left(=\frac{\beta r U_{\max}}{\nu_f}\right)$ is the local Reynolds number, M $\left(=\sqrt{\frac{\sigma B_0^2}{\rho_f \nu_f}}\right)$ is the magnetic number, Pr $\left(=\frac{\nu_f C_p}{k_f}\right)$ is the Prandtle number, R $\left(=\frac{16\sigma^* T_w^3}{3k^*(\rho c_p)_f}\right)$ is the radiation parameter, Ec $\left(=\frac{U_{\max}^2}{T_w c_p}\right)$ is the Eckert number, Df $\left(=\frac{K_T D_B C_w}{\nu_f T_w C_s c_p}\right)$ is the Dufour parameter, Sc $\left(=\frac{\nu_f}{D_B}\right)$ is the Schmidt number, Sr $\left(=\frac{K_T D_B T_w}{\nu_f C_w T_w}\right)$ is the Soret number, Br (=PrEc) is the Brinkman number, Δ $\left(=\frac{R_d D_B C_w}{k_f}\right)$ is the diffusion parameter, R_d is the molar gas constant, A $\left(=\frac{\delta}{\beta}\right)$ is the temperature slip, and m $\left(=\frac{\gamma}{\beta}\right)$ is the friction wall coefficient.

Engineering Interest Parameters. The physical parameters such as the skin friction coefficient, the Nusselt number Nu, and the Sherwood number Sh are used to quantify the flow, heat, and mass transfer rate characteristics of a nanofluid interacting with a boundary, respectively. The preceding are offered as the generalized forms of various physical quantities:

$$\left.\begin{aligned} C_f &= \frac{\mu_0}{\rho_f U_{\max}^2}\left[1 + \Pi^2\left(2\left(\frac{\partial U_r}{\partial r}\right)^2 + \frac{1}{r^2}\left(\frac{\partial U_r}{\partial \theta}\right)^2 + \frac{2U_r^2}{r^2}\right)\right]^{0.5(n-1)}\left(\frac{\partial U_r}{\partial \theta}\right)\Bigg|_{\theta=\beta} \\ \mathrm{Nu} &= -\frac{1}{T_w}\left[1 + \frac{16\sigma^* T_w^3}{3k^*(\rho c_p)}\right]\left(\frac{\partial T}{\partial \theta}\right)\Bigg|_{\theta=\beta} \\ \mathrm{Sh} &= -\frac{1}{C_w} r\left(\frac{\partial C}{\partial r}\right)\Bigg|_{\theta=\beta} \end{aligned}\right\} \quad (16)$$

The dimensionless notation of eq 16 becomes

$$\left.\begin{aligned} C_f &= \frac{1}{\mathrm{Re}}[[(1 + \mathrm{We}^2(4\beta^2 f^2(1) + f'^2(1)))^{0.5(n-1)}]f'(1)] \\ \mathrm{Nu} &= -\frac{1}{\beta}(1+R)\Theta'(1) \\ \mathrm{Sh} &= -\frac{1}{\beta}\Psi'(1) \end{aligned}\right\} \quad (17)$$

3. SOLUTION PROCEDURE

The Keller box method (KBM) numerical quadrature[51] is implemented to tickle the modeled equations. Due of its quick convergence, it is preferred over many other methods. The Keller box approach is inherently stable and convergent to the second order. It passes the von Neumann stability test, which specifies the standard for numerical solution convergence with respect to actual PDE solutions while taking consistency and numerical solution stability into account. Since the modeled governing equation is converted from PDEs by employing similarity transformations to coupled ordinary differential structures, eqs 11−13 describe the velocity, temperature, and concentration fields, respectively, in dimensionless form subjected to the boundary conditions (eq 14). Because the obtained differential equations are complex, finding a solution using analytical methods is an extremely laborious operation. As a result, the numerical approaches are thought to be the most effective at discovering issue simulations. We have adopted a computational technique while keeping in mind the benefits of a numerical scheme in terms of reduced

https://doi.org/10.1021/acsomega.2c05937
ACS Omega 2023, 8, 9121−9136

computational and temporal expenses. Spatial nodes like ξ are set to 0.05 for the computation. In this calculation, the convergence threshold was fixed at 10^{-6} to increase the precision of the result. The outcomes are obtained in a decent amount of time, and the coding is straightforward. Second-order convergence and unconditional stability characterize the implicit Keller box technique. The shooting method adopted for such problems is unstable and reliant on the initial guess, in contrast to the Keller box technique. The computational system is a package that is widely utilized by users with a wide range of skill levels in industry, research, and education. The controlling eqs 11−13 are solved numerically by MATLAB in the current article. The shooting approach is a procedure for transforming the governing equation into a form that is practical, such as eqs 11−13.

The Keller box approach includes the following steps:

Introducing new variable

$$x_1 = f,\ x_2 = f',\ x_3 = f'' \tag{18}$$

$$\begin{aligned} x_3' = &-\frac{4\beta^2 x_2}{Y_1} - \frac{2\beta \mathrm{Re} x_1 x_2}{X_1 Y_1} + \frac{\beta^2 M^2 x_2}{X_1 Y_1} \\ &- \frac{(n-1)\mathrm{We}^2 Y_2}{X_1 Y_1}[3x_2 x_3^{\,2} + 32\beta^2 x_1 x_2 x_3 + 64\beta^4 x_2 x_1^{\,2}] \\ &- \frac{(n-1)(n-3)\mathrm{We}^4 Y_3}{X_1 Y_1}[x_2^{\,2} x_3^{\,2} + 16\beta^2 x_1 x_2^{\,3} x_3 \\ &+ 32\beta^4 x_1^{\,3} x_2 x_3 + 16\beta^4 x_1^{\,2} x_2^{\,3} + 64\beta^6 x_1^{\,6} x_2 - 4\beta^2 x_2^{\,5}] \end{aligned} \tag{19}$$

$$x_4 = \Theta,\ x_5 = \Theta' \tag{20}$$

$$\begin{aligned} x_5' = &-\frac{Pr(N_B x_5 x_7 + N_T x_5^{\,2})}{(1+R)} - \frac{\mathrm{PrEc} Y_1}{(1+R)} - \frac{\beta^2 M \mathrm{PrEc} x_1^{\,2}}{(1+R)} \\ &- \frac{Df \mathrm{Pr} x_5'}{(1+R)} \end{aligned} \tag{21}$$

where

$$\begin{bmatrix} Y_1 = [1 + \mathrm{We}^2(4\beta^2 x_1^{\,2} + x_2^{\,2})]^{0.5(n-1)} \\ Y_2 = [1 + \mathrm{We}^2(4\beta^2 x_1^{\,2} + x_2^{\,2})]^{0.5(n-3)} \\ Y_3 = [1 + \mathrm{We}^2(4\beta^2 x_1^{\,2} + x_2^{\,2})]^{0.5(n-1)} \\ X_1 = [1 + (n-1)\mathrm{We}^2 Y_2 x_2] \end{bmatrix} \tag{22}$$

$$x_6 = \Psi,\ x_7 = \Psi' \tag{23}$$

$$x_6' = -\mathrm{SrSc} x_5' \tag{24}$$

The system is discretized utilizing average values for the functions and central differences for the derivatives as

$$(x_1)_{j-1/2} = \frac{(x_1)_j + (x_1)_{j-1}}{2} \tag{25}$$

$$(x_2)_{j-1/2} = \frac{(x_1)_j - (x_1)_{j-1}}{\Delta x} \tag{26}$$

By using Newton's approach, the nonlinear difference equations (eqs 19−24) are linearized as follows:

$$(x_1)_j^{i+1} = (x_1)_j^{\,i} + \delta(x_1)_j^{\,i} \tag{27}$$

$Ay = c$ is employed to illustrate the resulting linear system. Here

$$\begin{bmatrix} [A_1] & [C_1] & & & & & \\ [B_1] & [A_2] & [C_2] & & & & \\ \ddots & \ddots & \ddots & & & & \\ & & & [B_{J-1}] & [A_{J-1}] & [C_{J-1}] & \\ & & & & [B_J] & [B_J] & \end{bmatrix} \begin{bmatrix} [\delta_1] \\ [\delta_2] \\ \vdots \\ [\delta_{J-1}] \\ \delta_J \end{bmatrix} = \begin{bmatrix} [c_1] \\ [c_2] \\ \vdots \\ [c_{J-1}] \\ c_J \end{bmatrix} \tag{28}$$

By adopting the block LU-factorization technique in MATLAB, the system (eq 28) is solved numerically. The solution vector is adjusted, and the procedure is repeated until the required accuracy of 10^{-6} is reached.

4. CODE AUTHENTICITY CHECK

The numerical findings are confirmed in Table 1 by comparison with the findings of Shukla et al.[13] and Moradi et al.[52] that have already been published. The schematic view of Table 1 is also provided for the clarity of the comparison in Figure 2. The numerical outcomes to construct the dimensionless velocity data exhibit excellent agreement to four decimal places. This evaluation supports the study's findings and gives information for modeling and constructing various engineering procedures.

Table 1. Comparative Assessment of the Current Findings for $f(\xi)$[a] with Shukla et al.[13] and Moradi et al.[52]

ξ	Moradi et al.[52]	Shukla et al.[13]	Keller box outcomes
0	1	1	1
0.1	0.97923570	0.97923570	0.97929012
0.2	0.91926588	0.91926586	0.91925980
0.3	0.82653366	0.82653367	0.82643290
0.4	0.71022116	0.71022117	0.71022879
0.5	0.58049946	0.58049936	0.58048990
0.6	0.44693507	0.44693495	0.44693901
0.7	0.31740845	0.31740834	0.31740190
0.8	0.19764115	0.19764102	0.19769830
0.9	0.09120427	0.09123032	0.09123023
1.0	0	0	0

[a]When Re = 110, β = 3°, We = 0, or n = 1, M = 0.

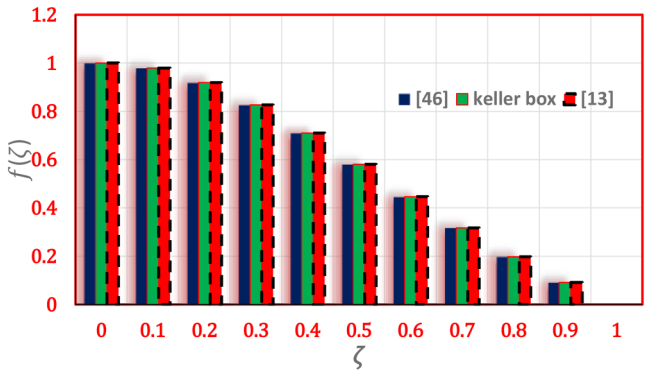

Figure 2. Schematic view of Table 1 for velocity plotted against dimensionless angle ξ.

https://doi.org/10.1021/acsomega.2c05937
ACS Omega 2023, 8, 9121−9136

5. RESULTS AND DISCUSSION

The present segment is devoted to the study of numerical results for several active parameters such as Re (=0, 50, 100, 150), the frictional wall parameter m (=1, 2, 3, 4), the magnetic field parameter M (=1, 2, 3, 4), the Prandtl number Pr (=6, 6.5, 7), the thermophoresis parameter N_T (=0.2, 0.4, 0.6), the Brownian diffusion parameter N_B (=0.2, 0.4, 0.6), the Dufour number Df (=0.2, 0.3, 0.4), the radiation parameter R (=0.2, 0.5, 0.8), the Schmidt number Sc (=0.2, 0.3, 0.4), the Soret number Sr (=0.2, 0.3, 0.4), the Brinkman number Br (=0.2, 0.3, 0.4), and the diffusion number Δ (=0.4, 1.4, 2.4). The physical performance of these results is discussed and projected using Figure 3. The ultimate focus is on investigating

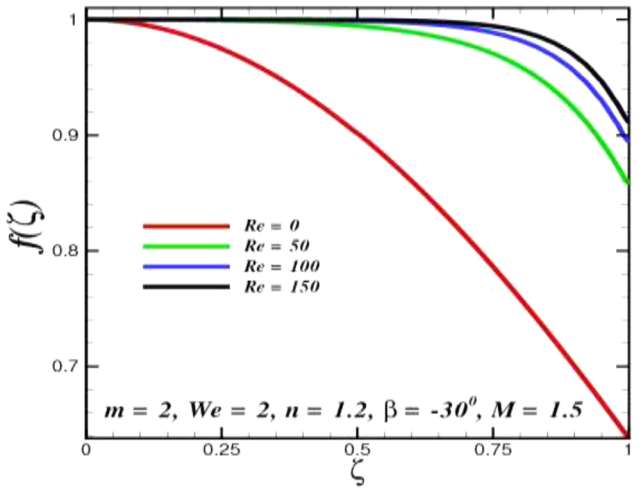

Figure 3. Deviation of velocity curves with augmented Reynold number Re (convergent channel case).

how the relevant parameters affect the flow pattern, the thermal field, the nanoparticle concentration, and the entropy rate of production in both convergent and divergent channels. This section is further divided into four subsections. For this analysis, the wedge angle is kept fixed at $\beta = -30°$ (for the converging case) and $\beta = 30°$ (for the diverging case). It is important to note that the model's outcomes are unaffected by the new formulation, even though small variations may appear due to computation. For instance, we have merely rewritten the dimensionless constitutive equations in terms of the dimensionless numbers stated in a way that is more compatible with the original idea.

5.1. Flow Analysis. The significance of the inertial term (Reynold number Re) on the dimensionless velocity distribution $f(\xi)$ inside converging and diverging channels is depicted in Figures 3 and 4, respectively. Here, remember that the flow rate is maintained the same as per the wall friction boundary conditions. As illustrated in Figure 3, the superiority of the inertial force triggers an increase in Re to maximize the velocity in the convergent channel. The relative strength of viscosity and inertia forces are quantified by the Reynolds number. Inertial forces grow as the Reynolds number increases. This happens due to the greater inertial flow and the narrowing of the wall together providing a pressure that accelerates the flow. The significance of this can be understood as follows: as viscosity increases, a greater pressure gradient is needed to maintain a certain flow rate. As a result, the outflow velocity increases, and the inflow velocity at the center does as well.

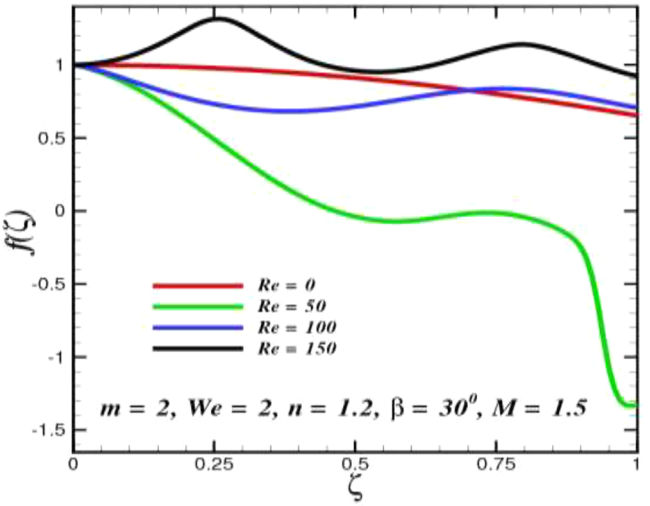

Figure 4. Deviation of velocity curves with augmented Reynold number Re (divergent channel case).

Figure 4 demonstrates that for an increasing Reynolds number Re, as the mobility tends to diminish for the diverging channel because of the higher inertial forces on the walls. Consequently, the inflow region's velocity increases in magnitude, which is paralleled by an increase in the outflow region's velocity. It is evident that the flow rate increases as the Reynolds number increases, although the effect is more pronounced at the centerline and has a negative consequence for the flow in diverging channels. The presence of flow reversal or a backflow/inflow zone is indicated by a negative nondimensional velocity value. A similar trend for the negative trend in the divergent channel against greater channel angle β = 30° and strong inertial forces was observed by Garimella et al.[41] There is a critical angle at which flow reversal occurs because the flow reverses when the angle is near β = 30°. Figures 5 and 6 provide an illustration of the nanofluid velocity in the channel because of the friction coefficient $m \geq 0$. These statistics suggest that the fluid flow is significantly impacted by surface roughness. Since the pressure gradient of the two-phase

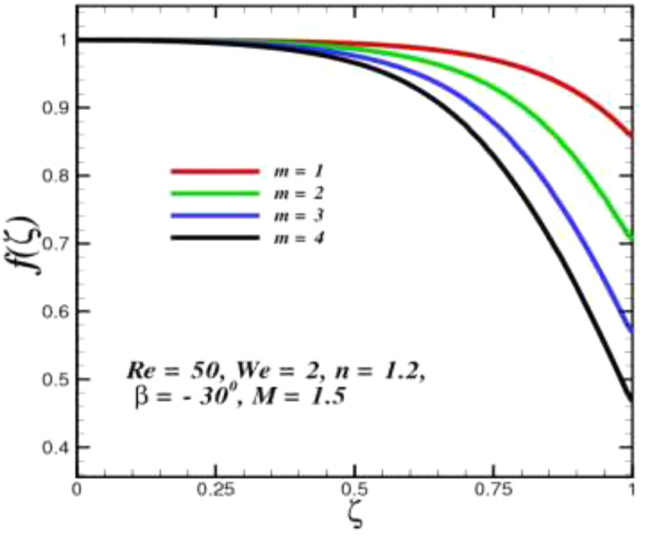

Figure 5. Deviation of velocity curves with augmented wall friction coefficient m (convergent channel case).

https://doi.org/10.1021/acsomega.2c05937
ACS Omega 2023, 8, 9121−9136

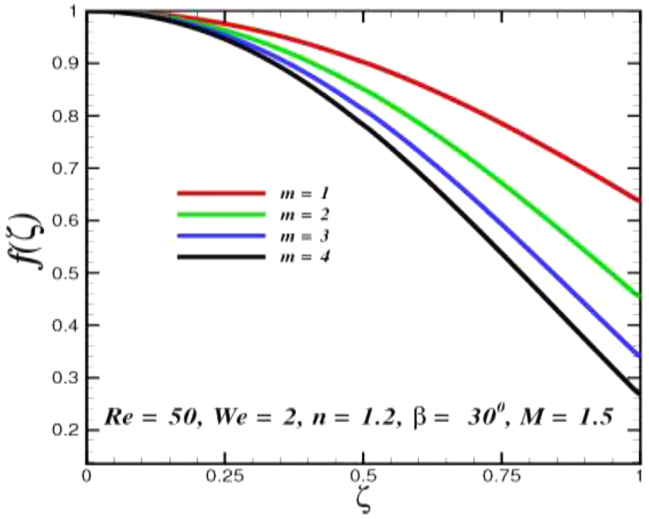

Figure 6. Deviation of velocity curves with augmented wall friction coefficient m (divergent channel case).

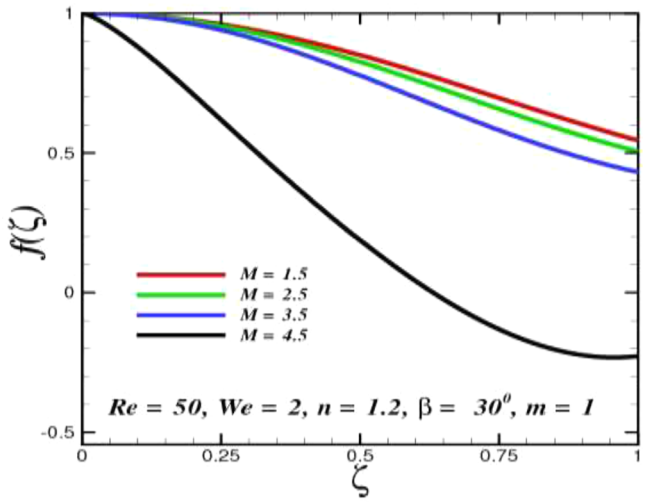

Figure 8. Deviation of velocity curves with augmented magnetic field parameter M (divergent channel case).

flow is one of the main factors in the design and operation of nuclear power systems, the wall friction model is another constitutive model that is essential for channel flow modeling. When it comes to the effectiveness of passive heat removal systems that exhibit the two-phase natural circulation at low velocity, a precise estimate of the wall friction is crucial. Therefore, an accurate modeling of the wall friction of the channel flow under a wide range of potential flow circumstances is crucial for converging diverging channel safety analysis. In both scenario velocity of the fluid is lower against wall friction. Nearly similar behavior for shear thinning fluid velocity was observed by Nagler.[49] The Lorentz force is augmented by a larger estimation of the magnetic variable. As a result, the resistance is strengthened. The outcome is a decrease in velocity $f(\xi)$. The considerable influence of magnetic number on velocity profiles inside converging/diverging channels is shown in Figures 7 and 8, respectively. The result is extremely dramatic, since fluid elements close to the wall can be seen accelerating to speeds that are faster than the centerline velocity in convergent channels. More significantly, flow separation in divergent channels may be totally suppressed by the acceleration brought by the magnetic forces. In fact, at greater values of the magnetic parameter, it becomes apparent that the streams appear in the channel's center. Additionally, it is noted that as M increases, the flow within the wedge degenerates. This happens as a response to the Lorentz force being enhanced by greater levels of M. As the Lorentz force increases, nanoparticles become more resistant, and the velocity of the Carreau liquid decreases in both channels.

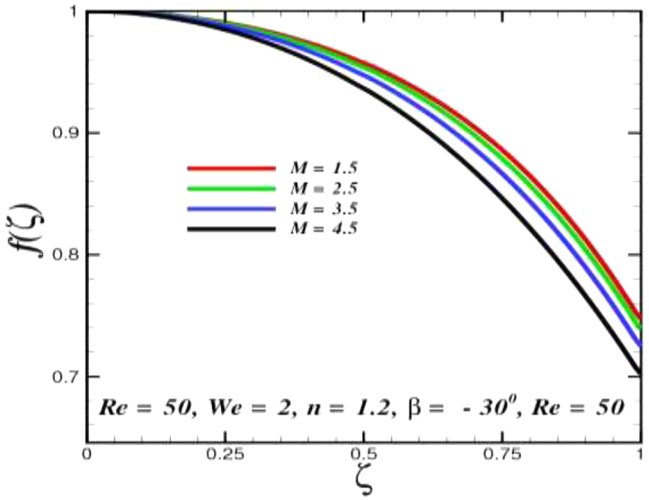

Figure 7. Deviation of velocity curves with augmented magnetic field parameter M (convergent channel).

5.2. Thermal Distribution. Effect of the involved physical parameter in thermal energy equation is evaluated in Figures 9−14. Figure 9 highlights the reduction of temperature with higher Prandtl numbers. Because the Prandtl number exhibits reversible action with thermal conductivity, it maximizes the amount of heat that may be transferred while also causing a reduction in the thickness of the thermal layer. The

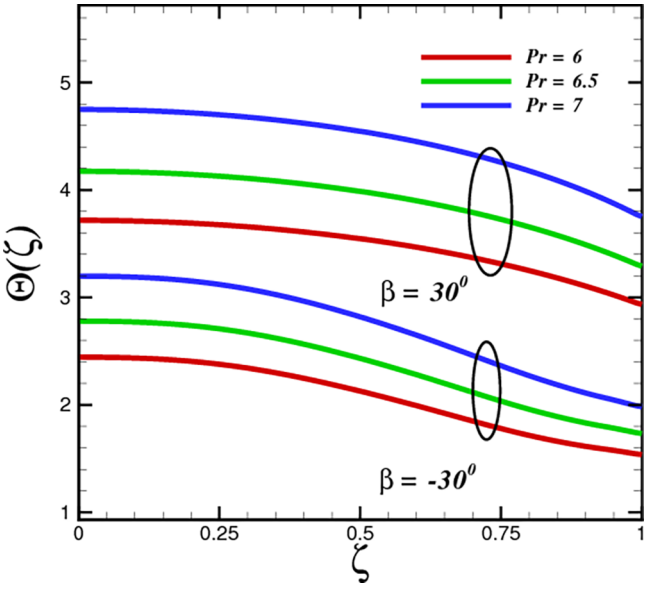

Figure 9. Deviation of temperature curves with augmented Prandtl number Pr (convergent/divergent channel) when We = 1, n = 1.6, Df = 0.5, R = 0.2, N_B = 0.4, N_T = 0.2, M = 2, Ec = 0.1, and A = 1.

https://doi.org/10.1021/acsomega.2c05937
ACS Omega 2023, 8, 9121−9136

temperature then becomes a condensed consequence of the Prandtl number in the wedge geometry. This is because the augmented thermal diffusivity associated with increasing Pr values enables the temperature to degrade. Since Pr admits an inverse relationship to thermal diffusivity, increasing Pr causes a reduction in the thermal diffusivity, which reduces the flow field's temperature in an oblique channel. Thermophoresis is a mechanism that causes the bulk movement of nanoparticles because of temperature differences. As shown in Figure 10, this

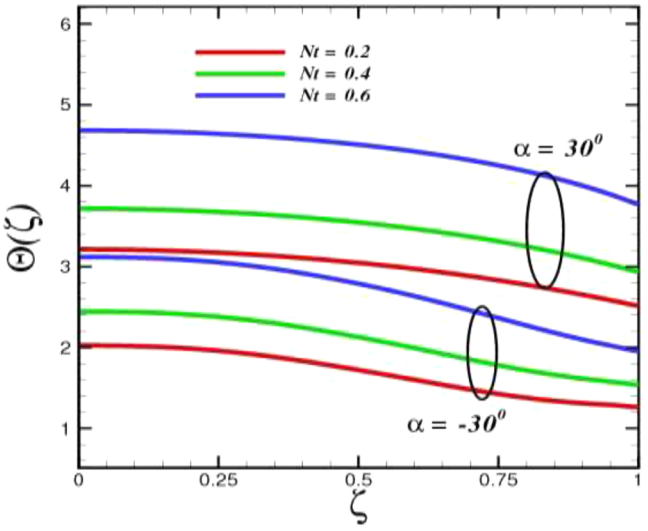

Figure 10. Deviation of temperature curves with augmented thermophoresis parameter N_T (convergent/divergent channel) when Pr = 6.2, We = 1, n = 1.6, Df = 0.5, R = 0.2, N_B = 0.4, M = 2, Ec = 0.1, and A = 1.

causes the fluid to drift more quickly, which raises the temperature of the liquid in the stream. Physically, the thermophoresis parameter develops the thermophoresis force that drives the nanomaterials from a hotter portion to a cold region, improving the temperature distribution and the thickness of the thermal layer. Figure 11 analyzes the Brownian motion parameter fluctuations and their effect the temperature distributions. According to the observations, when nanoparticles move more randomly, they absorb more heat, lowering the fluid stream's temperature. Due to the existence of nanoparticles, Brownian motion occurs in the nanofluid model, which controls the fluid's velocity and heat transmission characteristics. The temperature profile expands because of the radiation number. The kinetic energy of the liquid increases with the stronger radiation parameter R, and the kinetic energy increases the fluid's temperature $\Theta(\xi)$, as shown in Figure 12. It is worth mentioning that a stronger value of R enables the temperature in the channel to grow, which causes the thickness of the thermal boundary layer to increase at the same time. It is evident that an increase in the value of the radiation parameter enables the temperature to elevate while also elevating the thermal layered boundary, as the physiological parameter dictates the relative contribution of heat transfer by conduction to radiation transfer. Furthermore, the temperature escalates in the divergent channel more rapidly as compared to the convergent channel. Physically, escalations in temperature in the divergent channel dominate because the large opening angle of the channel tends to reduce the elasticity of the fluid. Furthermore, the existence of

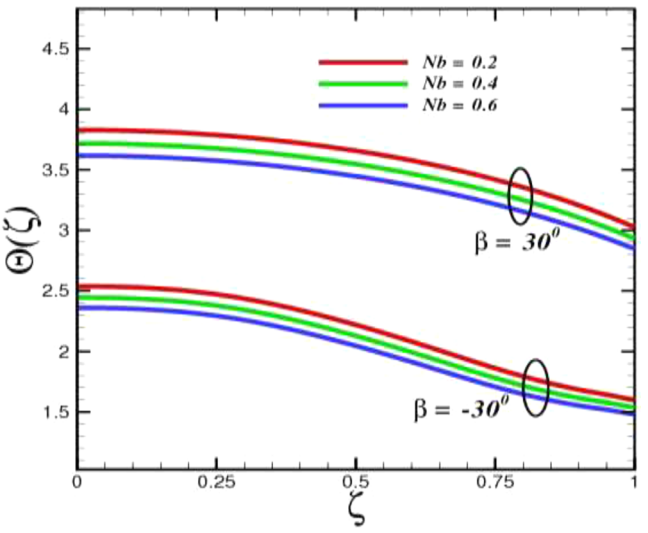

Figure 11. Deviation of temperature curves with augmented Brownian diffusion number N_B (convergent/divergent channel) when We = 1, n = 1.6, Df = 0.5, R = 0.2, N_T = 0.2, Pr = 6.2, M = 2, Ec = 0.1, and A = 1.

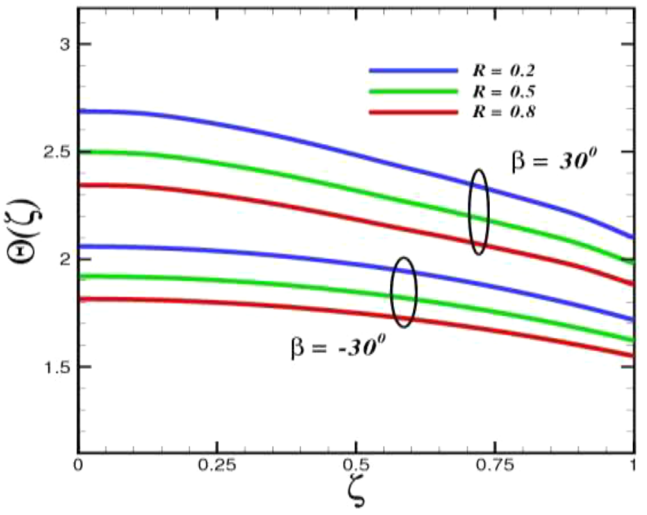

Figure 12. Deviation of temperature curves with augmented radiation parameter R (convergent/diverging channel) when We = 1, n = 1.6, Df = 0.5, N_T = 0.2, Pr = 6.2, N_B = 0.4, Ec = 0.1, and A = 1.

nanoparticles mixed with fluid in the convergent channel has a negative impact on the heat transfer rate, while the divergent channel's impact on the heat transfer rate is positive. The temperature field solutions are illustrated in Figure 13 for distinct values of the Dufour number Df. It turns out that as Df increases to its maximum, the fluid's temperature increases. The temperature curves exhibit dominant behavior for divergent channel as compared to the converging portion. It is pretty apparent that the diffusion−thermo effects can be summarized as the Dufour coefficient. The Dufour effect, also termed the diffusion−thermo effect, is a result of the concentration gradient inducing energy flux. The transport of energy improves, and the thermal gradient diminishes when the Dufour parameter increases. The Dufour effect is a result of a concentration gradient inducing a heat flux over a region. Physically speaking, it is demonstrated that as Df improves, more heat flow results from an increase in a temperature gradient, which promotes the increase in temperature.

https://doi.org/10.1021/acsomega.2c05937
ACS Omega 2023, 8, 9121−9136

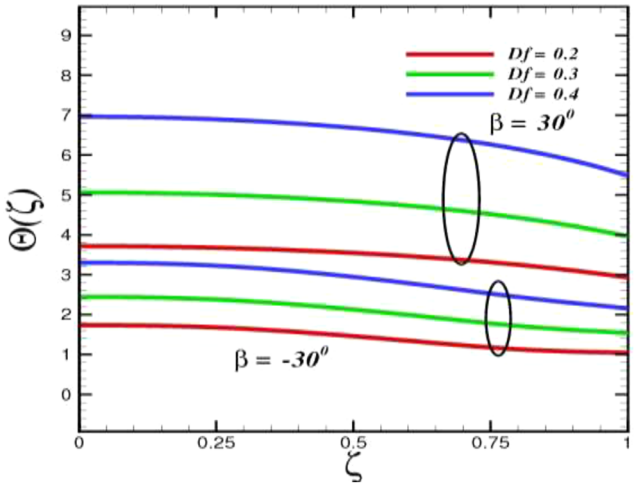

Figure 13. Deviation of temperature curves with augmented Dufour number Df (divergent/diverging channel) when We = 1, n = 1.6, N_T = 0.2, N_B = 0.4 R = 0.2, N_T = 0.2, Pr = 6.2, M = 2, Ec = 0.1, and A = 1.

Increased temperature is the consequence of a greater concentration gradient because the Dufour number emerges from the concentration gradient in the energy equation. It is also worth mentioning that the center of the channel experiences the greatest temperature changes. The temperature change is hardly noticeable close to the walls. The function of the magnetic number M on temperature $\Theta(\xi)$ is shown in Figure 14. The magnetic number provides an illustration of

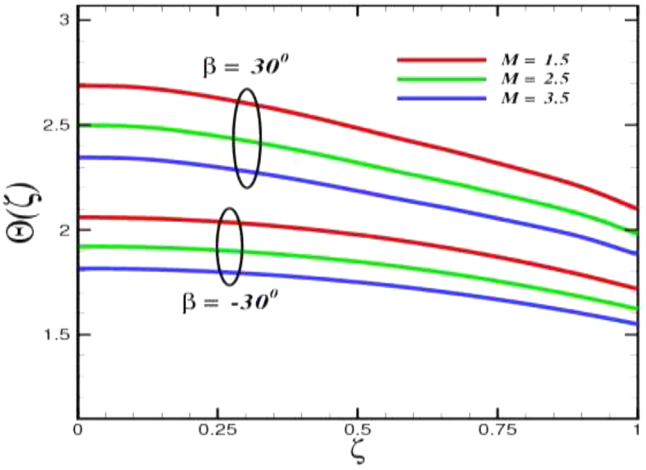

Figure 14. Deviation of temperature curves with augmented magnetic parameter M (convergent/diverging channel), when We = 1, n = 1.6, Df = 0.5, R = 0.2, N_T = 0.2, Pr = 6.2, N_B = 0.4, Ec = 0.1, and A = 1.

how electromagnetic force and viscous force are related. Physically, the electric vortices in the flow field increase as the magnetic field increases (raising the magnetic number). These electric vortices will cause resistance in the fluid, which will slow it down. This impedance generates more friction, and more friction results in more dissipation, which leads to more heat transfer in the divergent channel. According to graphic, the temperature in a convergent channel is a decreasing function of the magnetic number as compared to diverging flow. This is because a perpendicular magnetic field induces the Lorentz force, a resistive force in an electrically conducting fluid. This force generates frictional force between the fluid's layers, which lowers the temperature of the fluid and causes resistance inside its particles.

5.3. Nanoparticles Concentration. The concentration profile $\Psi(\xi)$ is plotted against the Schmidt number Sc, and a significant variation is seen in Figures 15 and 16. The

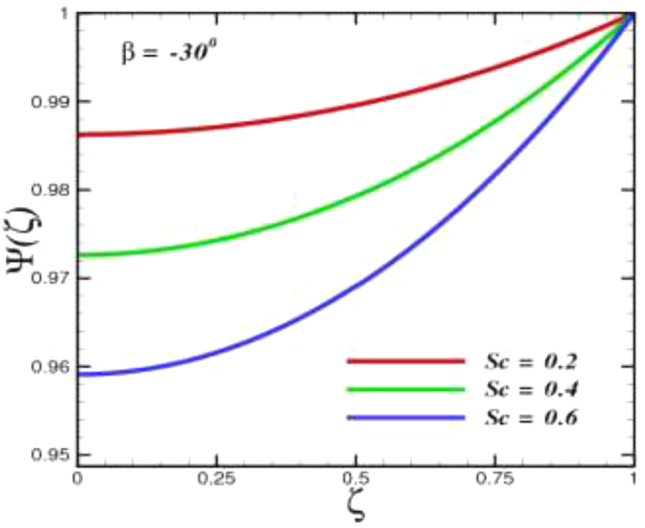

Figure 15. Deviation of concentration curves with augmented Schmidt number Sc (convergent channel) when We = 1, n = 1.6, R = 0.2, N_B = 0.4, N_T = 0.2, Pr = 6.2, Df = 0.5, M = 2, and Sr = 0.2.

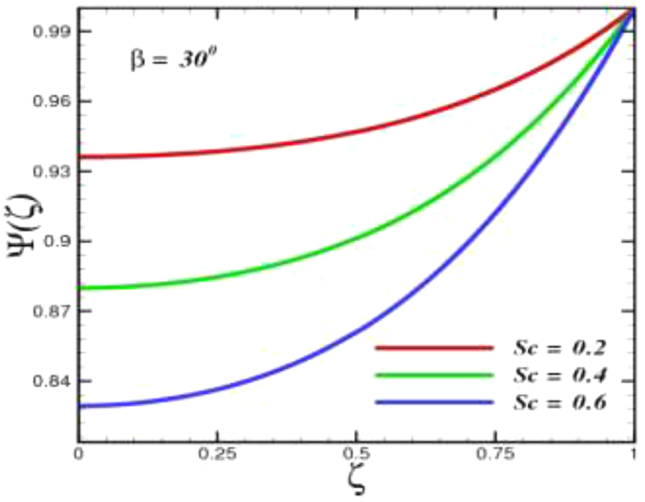

Figure 16. Deviation of concentration curves with augmented Schmidt number Sc (divergent channel) when We = 1, n = 1.6, R = 0.2, N_B = 0.4, N_T = 0.2, Pr = 6.2, Df = 0.5, M = 2, and Sr = 0.2.

nanoparticle concentration is evaluated with large channel opening angle $\beta = -30°$ and $\beta = 30°$. The significance of the Schmidt number Sc on the heat region is illustrated. The mass diffusivity D_B and the Schmidt number Sc are inversely related. Therefore, the increase in Sc indicates a decline in the mass diffusivity, which displays a pattern of degradation in the concentration field. If the Schmidt number is less than 1, momentum diffusivity will take precedence over mass diffusivity. This has a different effect in the convergent and divergent channels, where it is perceived that decreased momentum diffusivity causes an increase in the concentration of nanoparticles. Physically, as the Schmidt number grows, mass diffusion declines, decreasing the concentration. At the

https://doi.org/10.1021/acsomega.2c05937
ACS Omega 2023, 8, 9121−9136

central point of the channel, a sharp concentration decline is seen. This phenomenon results from stronger viscous forces. It is evident from Figures 17 and 18 that an elevation in species

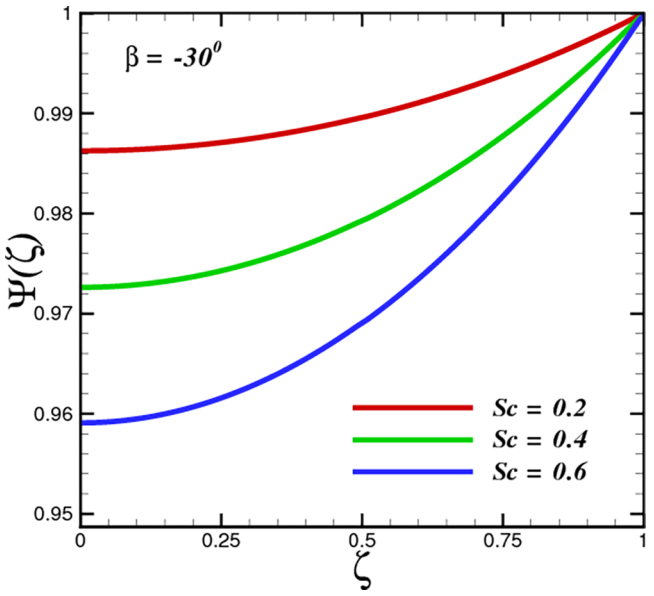

Figure 17. Deviation of concentration curves with augmented Soret number Sr (convergent channel) when We = 1, n = 1.6, R = 0.2, N_B = 0.4, N_T = 0.2, Pr = 6.2, Df = 0.5, M = 2, and Sc = 0.2.

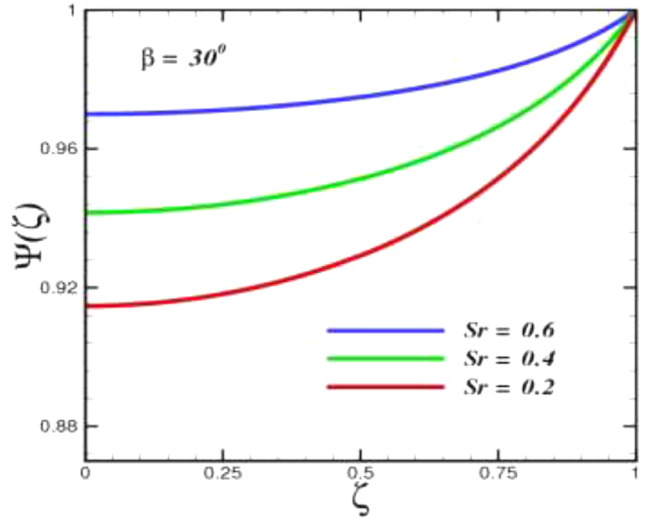

Figure 18. Deviation of concentration curves with augmented Soret number Sr (divergent channel), when We = 1, n = 1.6, R = 0.2, N_B = 0.4, N_T = 0.2, Pr = 6.2, Df = 0.5, M = 2, and Sc = 0.2.

concentration occurs due to an increase in Soret number Sr. A heat gradient in concentration expression yields the Soret number Sr. The concentration zone is enhanced by this heat gradient. The enhanced molar mass diffusivity suggested by the improved Soret impact could explain the increase in concentration. Following the description of the Soret number, a rise in Soret effect signifies an increase in molar mass diffusion rate. The spike in concentration is driven on by a boost in molecular mass diffusivity. This reveals that the Soret number tends to elevate the fluid's species concentration.

5.4. Entropy Evaluation. The goal of the current computational endeavor is to understand the irreversibility in terms of entropy production S_G brought on by an inadequate temperature inside the convergent/divergent channel due to heat transfer, mass transfer, fluid friction, and ohmic heat. Figures 19 and 20 scrutinize the significant impact of the

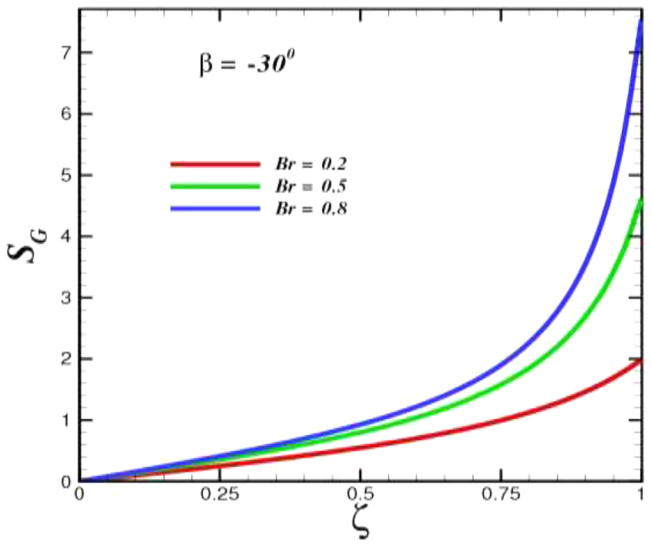

Figure 19. Deviation of entropy curves with augmented Brinkman number Br (convergent channel) when We = 1, n = 1.6, R = 0.2, Pr = 6.2, Δ = 0.5, and M = 2.

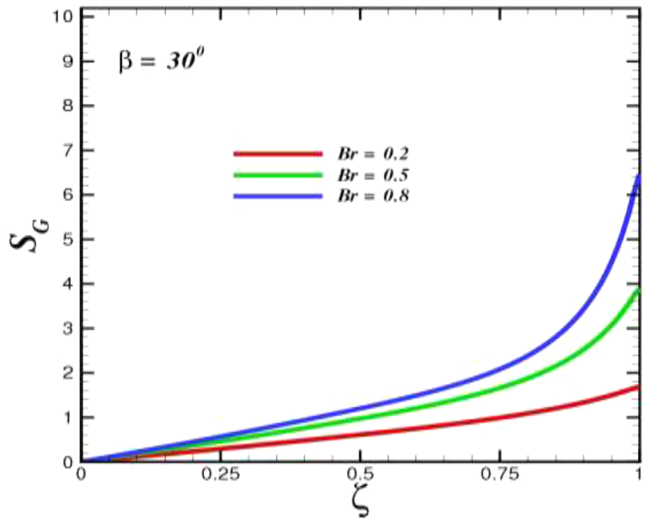

Figure 20. Deviation of entropy curves with augmented Brinkman number Br (Divergent channel) when We = 1, n = 1.6, R = 0.2, Pr = 6.2, Δ = 0.5, and M = 2.

Brinkman number on entropy in a converging/diverging channel. A raised Brinkman number enhances the viscous force, which raises the probability of kinematic collision. Therefore, the entropy rate increased. Furthermore, it is evident from sketches the entropy growth in the divergent channel is dominant. Physically, the irreversibility of viscous dissipation overtakes the irreversibility of heat transmission as the Brinkman number grows. The Brinkman number Br is a measure of the heat dissipated (generated) by viscous dispersion compared to the heat supplied by liquid molecules. Consequently, an increase in the Brinkman number demonstrates that a significant amount of heat is produced via viscous

https://doi.org/10.1021/acsomega.2c05937
ACS Omega 2023, 8, 9121−9136

dispersion compared to the heat transmitted by molecular conduction, which causes an increase in S_G. Figures 21 and 22

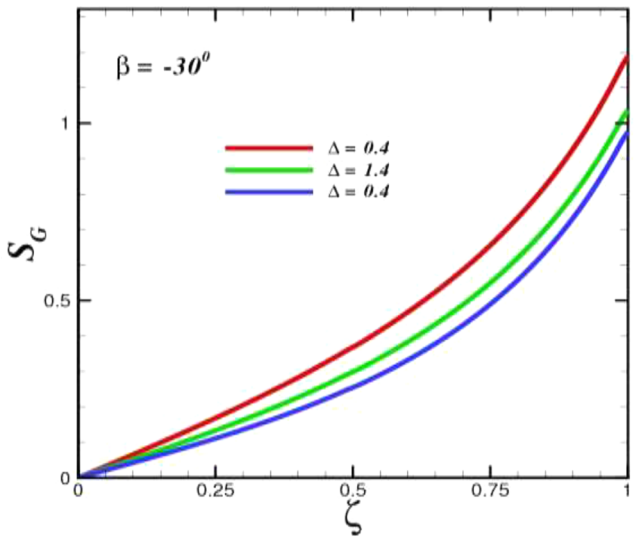

Figure 21. Deviation of entropy curves with augmented diffusion number Δ (convergent channel) when We = 1, n = 1.6, R = 0.2, Pr = 6.2, Br = 0.2, and M = 2.

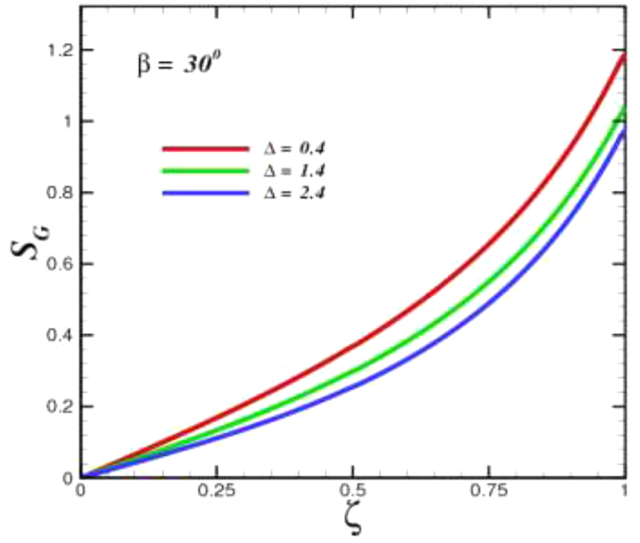

Figure 22. Deviation of entropy curves with augmented diffusion number Δ (divergent channel) when We = 1, n = 1.6, R = 0.2, Pr = 6.2, Br = 0.2, and M = 2.

highlight the entropy generation effect due to diffusion parameter Δ. Entropy generation improves for a better estimation of Δ. Due to an increase in diffusion, mass transfer irreversibility has a more significant impact than viscous dissipation irreversibility, resulting in entropy improvement. Entropy production is more prominent within the central core of the channel, while near the wall of the channel the consequences are reversed. The thermal radiation parameter R increases the wedge entropy due to radiant heat, as evident in Figures 23 and 24. The means that more heat is provided to the liquid with augmented radiant heat, causing the temperature and thermal boundary layer density to rise. This is because accumulation in the thermal radiation parameter

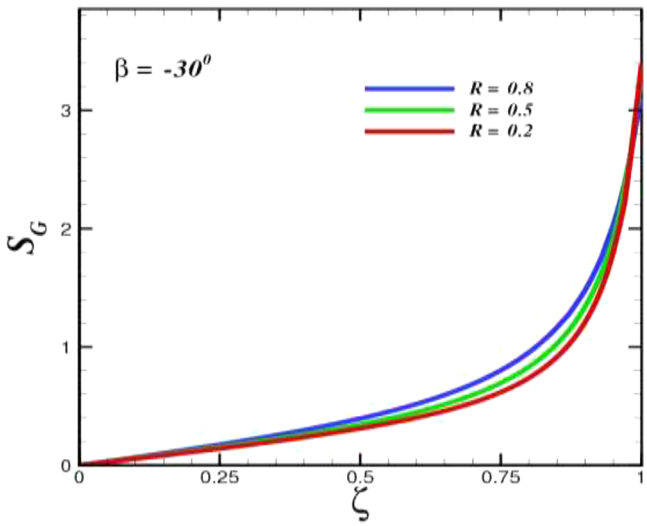

Figure 23. Deviation of entropy curves with augmented radiation number R (Convergent channel) when We = 1, n = 1.6, Δ = 0.5, Pr = 6.2, Br = 0.2, and M = 2.

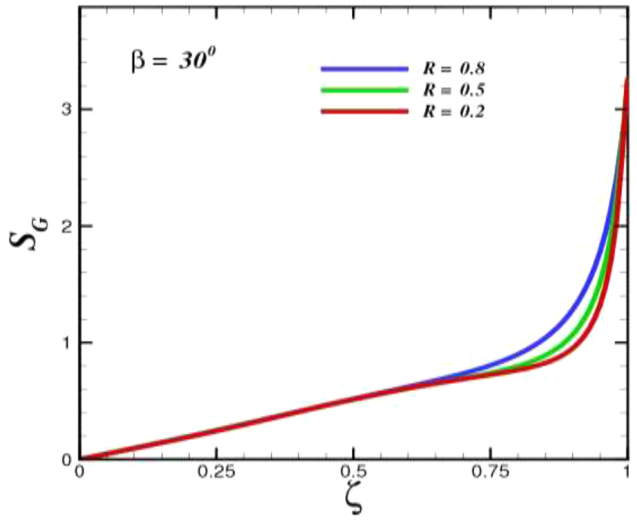

Figure 24. Deviation of entropy curves with augmented Radiation number R (divergent channel) when We = 1, n = 1.6, Δ = 0.5, Pr = 6.2, Br = 0.2, and M = 2.

causes the interaction in the thermal boundary layer to escalate. In addition, higher radiation parameter values heat the nanofluids significantly, increasing their temperature profile and their more pronounced thermal boundary layer width. The local entropy profile due to magnetic field strength M is observed in Figures 25 and 26. The magnetism factor is established for the relationship between electromagnetic force and viscosity. Because of the strong relationship between Lorentz force and magnetic force, which improves as the magnetic force, the retarding force also increases. Lorentz's force was created in a stream because of the magnetic force. Physically, higher values of M cause S_G to grow because higher fluid temperatures increase the resistive forces among liquid molecules. Magnetic entropy is produced more quickly when the magnetic number increases. The intensity of the Lorentz force is stronger in the vertical direction and smaller in the horizontal direction because the magnetic field is applied to the fluid flow in a horizontal direction. Magnetic entropy contours

https://doi.org/10.1021/acsomega.2c05937
ACS Omega 2023, 8, 9121−9136

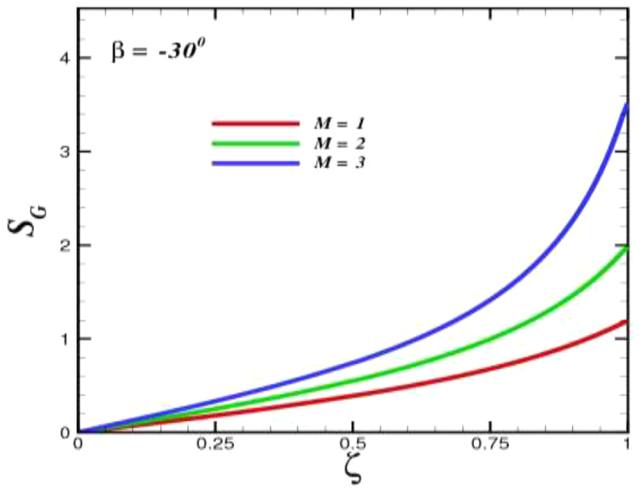

Figure 25. Deviation of entropy curves with augmented magnetic number M (convergent channel) when We = 1, n = 1.6, Δ = 0.5, Pr = 6.2, Br = 0.2, and R = 0.2.

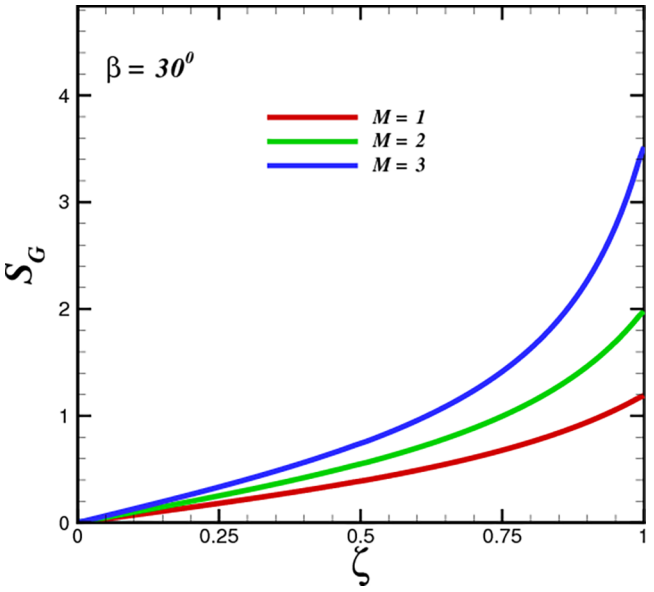

Figure 26. Deviation of entropy curves with augmented magnetic number M (divergent channel), when We = 1, n = 1.6, Δ = 0.5, Pr = 6.2, Br = 0.2, and R = 0.2.

are seen near the channel surface and bounds for the smallest value of the magnetic number. The channel where recirculating happens because of prolonged interference and Lorentz force is where the maximum rate of magnetic entropy formation occurs when the magnetic number increases. It is also known that magnetic entropy creation is lower for low thermal conductivity ratios and that heat transfer irreversibility predominates among irreversibility.

5.5. Table Discussion. Table 2 explains the comparative analysis of entropy formation within the wedge. The numerical results reveal that thermal distribution dominant within the divergent channel, which leads to loss of energy, and hence entropy increases. Due to rising Eckert numbers for diverging channels, the entropy generation profile is enhanced. For all the cases concerned, an increase in the radiation parameter improves the system's entropy generation. With an increase in the Brinkman number, the entropy generation becomes more

Table 2. Comparative Assessment of Entropy Production Rate in a Convergent−Divergent Channel

						S_G	
Br	We	n	M	R	Δ	$\beta = -30°$	$\beta = 30°$
0.4	1.0	1.1	2	0.1	0.5	2.1009	3.2490
0.5						3.4340	4.7561
0.6						5.2592	6.6143
0.4	1.0	1.1	2	0.1	0.5	1.2334	4.2082
	1.2					2.0268	4.0177
	1.4					3.3766	3.8443
0.4	1.0	1.1	2	0.1	0.5	2.4208	3.3914
		1.2				3.8443	3.8361
		1.4				3.4487	4.3843
0.4	1.0	1.1	2	0.1	0.5	2.5572	2.5424
			3			3.5503	3.5249
			4			6.6679	6.6123
0.4	1.0	1.1	2	0.1	0.5	5.2012	5.1506
				0.2		6.6679	6.6123
				0.3		8.6829	8.6489
0.4	1.0	1.1	2	0.1	0.5	7.3137	7.3039
					0.7	6.9926	6.9473
					0.9	6.7954	6.7440

prominent. In all concerned cases, the entropy of the system is dominate in the divergent channel. The values of entropy generation in this study illustrate that the irreversibility of the system is mainly dominated by flow friction. Keeping in view our previous study,[47] the entropy of the system is lower in the case of a large opening of the channel. The fact behind the entropy minimization is a large channel apex angle where the thermal characteristics are substantially higher. Table 3 is plotted to examine the comparative analysis of thermal distribution within converging and diverging channel against emerging parameters. The computational results infer that the thermal distribution is dominant in divergent channel.

6. CONCLUSION

As per the modeling perspective, a viscous dissipation model is developed for the interaction of the externally applied magnetics forces with the heat and mass transport process in a wedge-shaped convergent/divergent enclosure under the influence of Soret and Dufour effects. Entropy generation analysis is also carried out in this study, which is significant for developing a thermal system that not only generates the desired amount of output but also makes the best use of the available resources. To identify the mechanisms of irreversibility and to quantify the thermodynamic irreversibility prevailing in an inclined channel, the local entropy generation rate is obtained from the second law of thermodynamics. The entropy generation model specifically considers the contributions of heat transmission, mass transfer, and ohmic loss effects. The set of governing equations is handled numerically by a Keller box scheme. The primary analysis is based on the impact of pertinent parameters and the thermal design of the enclosure on the flow, thermal, and concentration distribution and entropy generation characteristics. The main accomplishments of the study are established in the following points.

1. The velocity of the Carreau liquid is elevated with Reynold's number in converging channel, while in diverging channel it is depressed.

https://doi.org/10.1021/acsomega.2c05937
ACS Omega 2023, 8, 9121−9136

Table 3. Computations Presenting the Temperature Distribution against Various Parameters in a Converging Channel and a Divergent Channel

									$\Theta(\xi)$	
Pr	We	n	N_B	N_T	Ec	Df	M	R	$\beta = -30°$	$\beta = 30°$
7	1.0	1.2	0.4	0.2	0.1	0.5	2	0.5	1.1038	1.2696
10									1.1617	1.3851
13									1.1802	1.5006
7	1.0	1.2	0.4	0.2	0.1	0.5	2	0.5	1.1050	1.2961
	1.2								1.1002	1.2696
	1.4								1.0392	1.2743
7	1.0	1.2	0.4	0.2	0.1	0.5	2	0.5	1.1328	1.2790
		1.4							1.1432	2.1687
		1.6							1.1564	2.2880
7	1.0	1.2	0.4	0.2	0.1	0.5	2	0.5	1.1326	2.0783
			0.6						1.1328	2.0784
			0.8						1.1330	2.0785
7	1.0	1.2	0.4	0.2	0.1	0.5	2	0.5	1.1328	1.2694
				0.4					1.1261	1.2693
				0.6					1.1230	1.2692
7	1.0	1.2	0.4	0.2	0.1	0.5	2	0.5	1.1934	1.2696
					0.2				1.2210	1.5391
					0.3				1.2271	1.8087
7	1.0	1.2	0.4	0.2	0.1	0.5	2	0.5	1.3029	1.3116
						0.6			1.4236	1.661
						0.7			1.5216	1.7959
7	1.0	1.2	0.4	0.2	0.1	0.5	2	0.5	1.1468	1.4230
							3		1.1268	1.3029
							4		1.1001	1.2961
7	1.0	1.2	0.4	0.2	0.1	0.5	2	0.5	1.2451	1.4230
								0.6	1.3450	1.5498
								0.7	1.6324	1.8882

2. Increasing the Re number causes the volume flux to concentrate at the channel's center in divergent flow. In these circumstances, the boundary layer thickness increases with the Re number.
3. Fluid velocity in the convergent channel is increased by a large Reynold number with greater channel angle (β), whereas the opposite behavior may occur in the divergent channel.
4. A negative value of nondimensional velocity indicates the presence of flow reversal or a backflow region with large divergent channel angle $\beta = 30°$.
5. There is a spike in the temperature and entropy rate for the radiation parameter.
6. The reverse trend is illustrated by the Soret and Schmidt numbers on the nanoparticle concentration.
7. The total entropy production is observed to increase for the Brinkman number, the magnetic field strength, and the diffusion parameter.
8. Entropy of the system can be minimized with a large channel angle.

■ ASSOCIATED CONTENT

Data Availability Statement

The author confirms that the data supporting the findings of this study are available within the manuscript.

■ AUTHOR INFORMATION

Corresponding Author

Hashim − *Department of Mathematics and Statistics, The University of Haripur, Haripur, Khyber Pakhtunkhwa 22620, Pakistan;* orcid.org/0000-0003-3663-8682; Email: hashim@math.qau.edu.pk

Authors

Sohail Rehman − *Department Mechanical Engineering, School of Material Sciences and Engineering, Georgia Institute of Technology, Atlanta, Georgia 30318, USA;* orcid.org/0000-0001-9713-4870

Siwar Ben Hadj Hassine − *Department of Computer Science, College of Science and Arts at Muhayel, King Khalid University, Abha, Asir 61421, Saudi Arabia*

Elsayed Tag Eldin − *Center of Research, Faculty of Engineering, Future University in Egypt, New Cairo, Cairo 11835, Egypt*

Syed Omer Shah − *Department of Mathematics, University of Peshawar, Peshawar, Khyber Pakhtunkhwa 25120, Pakistan*

Complete contact information is available at: https://pubs.acs.org/10.1021/acsomega.2c05937

Notes

The authors declare no competing financial interest.

■ ACKNOWLEDGMENTS

The authors extend their appreciation to the Deanship of Scientific Research at King Khalid University for funding this work through Large Groups Project under Grant RGP.2/25/43.

■ NOMENCLATURE

U_r Radial velocity (ms^{-1})

https://doi.org/10.1021/acsomega.2c05937
ACS Omega 2023, 8, 9121−9136

U_{max}	Maximum velocity (ms^{-1})
(r,θ, z)	Cylindrical coordinates
Π	Relaxation time parameter (s)
T	Fluid temperature (K)
T_w	Wall temperature (K)
C	Fluid concentration (kg m^{-3})
C_w	Wall concentration (kg m^{-3})
k_f	Thermal conductivity (Wm^{-1} K^{-1})
σ	Electrical conductivity
σ^*	Stefan−Boltzmann constant
B_0	Magnetic field (tesla, A/m)
μ_0	Dynamic viscosity (kg m^1 s^{-1})
ν	Kinematic viscosity (m^2 s^{-1})
D_B	Brownian diffusion
D_T	Thermophoresis diffusion
N'''	Entropy generation
K_T	Thermal diffusion
C_s	Concentration susceptibility
α	Channel semi-angle
m	Friction coefficient
Q	Volumetric flow rate
R_d	molar gas constant
A	Temperature slip
ξ	Dimensional variable
f	Dimensionless velocity
Θ	Dimensionless temperature
Ψ	Dimensionless concentration
Re	Reynold number
Pr	Prandtl number
We	Weissenberg number
N_b	Brownian diffusion parameter
N_t	Thermophoresis diffusion parameter
M	Magnetic number
Ec	Eckert number
Sc	Schmidt number
Sr	Soret number
R	Radiation number
Br	Brinkman number
Δ	Diffusion parameter
Df	Dufour number
Nu	Nusselt number
Sh	Sherwood number
C_f	Skin friction

REFERENCES

(1) Bejan, A. Entropy Generation Minimization: The New Thermodynamics of Finite-size Devices and Finite-time Processes. *J. Appl. Phys.* **1996**, *79* (3), 1191−1218.

(2) Rashidi, M. M.; Nasiri, M.; Shadloo, M. S.; Yang, Z. Entropy Generation in a Circular Tube Heat Exchanger Using Nanofluids: Effects of Different Modeling Approaches. *Heat Transfer Eng.* **2017**, *38* (9), 853−866.

(3) Seyyedi, S. M.; Dogonchi, A.S.; Hashemi-Tilehnoee, M.; Waqas, M.; Ganji, D.D. Entropy Generation and Economic Analyses in a Nanofluid Filled L-Shaped Enclosure Subjected to an Oriented Magnetic Field. *Appl. Therm. Eng.* **2020**, *168*, 114789.

(4) Mehryan, S. A. M.; Izadi, M.; Chamkha, A. J.; Sheremet, M. A. Natural Convection and Entropy Generation of a Ferrofluid in a Square Enclosure under the Effect of a Horizontal Periodic Magnetic Field. *J. Mol. Liq.* **2018**, *263*, 510−525.

(5) Turkyilmazoglu, M. Velocity Slip and Entropy Generation Phenomena in Thermal Transport Through Metallic Porous Channel. *J. Non-Equilib. Thermodyn.* **2020**, *45* (3), 247−256.

(6) Khan, N.; Riaz, I.; Hashmi, M. S.; Musmar, S. A.; Khan, S. U.; Abdelmalek, Z.; Tlili, I. Aspects of Chemical Entropy Generation in Flow of Casson Nanofluid between Radiative Stretching Disks. *Entropy* **2020**, *22* (5), 495.

(7) Hayat, T.; Khan, S. A.; Ijaz Khan, M.; Alsaedi, A. Theoretical Investigation of Ree-Eyring Nanofluid Flow with Entropy Optimization and Arrhenius Activation Energy between Two Rotating Disks. *Comput. Methods Programs Biomed.* **2019**, *177*, 57−68.

(8) Jeffery, G. B. L. The Two-Dimensional Steady Motion of a Viscous Fluid. *London Edinb. Dublin Philos. Mag. J. Sci.* **1915**, *29* (172), 455−465.

(9) Hamel, G. Spiralförmige Bewegungen zäher Flüssigkeiten. *Jahresber. Dtsch. Math.-Ver.* **1917**, *25*, 34−60.

(10) Nagler, J. Jeffery−Hamel Flow of Nano Fluid Influenced by Wall Slip Conditions. *J. Nanofluids* **2016**, *5* (6), 960−967.

(11) Makinde, O. D. Entropy-Generation Analysis for Variable-Viscosity Channel Flow with Non-Uniform Wall Temperature. *Appl. Energy* **2008**, *85* (5), 384−393.

(12) Makinde, O.; Bég, O. On Inherent Irreversibility in a Reactive Hydromagnetic Channel Flow. *J. Therm. Sci.* **2010**, *19*, 72−79.

(13) Shukla, N.; Rana, P.; Pop, I. Second Law Thermodynamic Analysis of Thermo-Magnetic Jeffery−Hamel Dissipative Radiative Hybrid Nanofluid Slip Flow: Existence of Multiple Solutions. *Eur. Phys. J. Plus* **2020**, *135* (10), 849.

(14) Weigand, B.; Birkefeld, A. Similarity Solutions of the Entropy Transport Equation. *Int. J. Therm. Sci. - INT J. THERM SCI* **2009**, *48*, 1863−1869.

(15) Basha, H.; Sivaraj, R. Entropy Generation of Peristaltic Eyring−Powell Nanofluid Flow in a Vertical Divergent Channel for Biomedical Applications. *Proc. Inst. Mech. Eng. Part E J. Process Mech. Eng.* **2021**, *235* (5), 1575−1586.

(16) Alam, M. S.; Khan, M. A. H.; Makinde, O. D. Magneto-Nanofluid Dynamics in Convergent-Divergent Channel and Its Inherent Irreversibility. *Defect Diffus. Forum* **2017**, *377*, 95−110.

(17) Faghih Aliabadi, M. A.; Jahangiri, A.; Khazaee, I.; Lakzian, E. Investigating the Effect of Water Nano-Droplets Injection into the Convergent-Divergent Nozzle Inlet on the Wet Steam Flow Using Entropy Generation Analysis. *Int. J. Therm. Sci.* **2020**, *149*, 106181.

(18) Raja, M. A. Z.; Tabassum, R.; El-Zahar, E. R.; Shoaib, M.; Khan, M. I.; Malik, M. Y.; Khan, S. U.; Qayyum, S. Intelligent Computing through Neural Networks for Entropy Generation in MHD Third Grade Nanofluid under Chemical Reaction and Viscous Dissipation. *Waves Random Complex Media* **2022**, *0* (0), 1−25.

(19) Fadodun, O. G.; Amosun, A. A.; Okoli, N. L.; Olaloye, D. O.; Durodola, S. S.; Ogundeji, J. A. Sensitivity Analysis of Entropy Production in Al2O3/H2O Nanofluid through Converging Pipe. *J. Therm. Anal. Calorim.* **2021**, *143* (1), 431−444.

(20) Chapman, S.; Cowling, T. G. *The Mathematical Theory of Non-Uniform Gases: An Account of the Kinetic Theory of Viscosity, Thermal Conduction and Diffusion in Gases*; Cambridge University Press: Cambridge, England, 1991.

(21) Mahdy, A. MHD Non-Darcian Free Convection from a Vertical Wavy Surface Embedded in Porous Media in the Presence of Soret and Dufour Effect. *Int. Commun. Heat Mass Transfer* **2009**, *36* (10), 1067−1074.

(22) Mahabaleshwar, U. S.; Nagaraju, K. R.; Vinay Kumar, P. N.; Nadagouda, M. N.; Bennacer, R.; Sheremet, M. A. Effects of Dufour and Soret Mechanisms on MHD Mixed Convective-Radiative Non-Newtonian Liquid Flow and Heat Transfer over a Porous Sheet. *Therm. Sci. Eng. Prog.* **2020**, *16*, 100459.

(23) Ren, Q.; Chan, C. L. Numerical Study of Double-Diffusive Convection in a Vertical Cavity with Soret and Dufour Effects by Lattice Boltzmann Method on GPU. *Int. J. Heat Mass Transfer* **2016**, *93*, 538−553.

(24) Hayat, T.; Aslam, N.; Alsaedi, A.; Rafiq, M. Numerical Analysis for Endoscope and Soret and Dufour Effects on Peristalsis of Prandtl Fluid. *Results Phys.* **2017**, *7*, 2855−2864.

(25) Okuyade, W. I. A.; Abbey, T. M.; Gima-Laabel, A. T. Unsteady MHD Free Convective Chemically Reacting Fluid Flow over a

https://doi.org/10.1021/acsomega.2c05937
ACS Omega 2023, 8, 9121−9136

Vertical Plate with Thermal Radiation, Dufour, Soret and Constant Suction Effects. *Alex. Eng. J.* **2018**, *57* (4), 3863−3871.
(26) Kafoussias, N. G.; Williams, E. W. Thermal-Diffusion and Diffusion-Thermo Effects on Mixed Free-Forced Convective and Mass Transfer Boundary Layer Flow with Temperature Dependent Viscosity. *Int. J. Eng. Sci.* **1995**, *33* (9), 1369−1384.
(27) Postelnicu, A. Influence of a Magnetic Field on Heat and Mass Transfer by Natural Convection from Vertical Surfaces in Porous Media Considering Soret and Dufour Effects. *Int. J. Heat Mass Transfer* **2004**, *47*, 1467−1472.
(28) Sheremet, M. A. The Influence of Cross Effects on the Characteristics of Heat and Mass Transfer in the Conditions of Conjugate Natural Convection. *J. Eng. Thermophys.* **2010**, *19* (3), 119−127.
(29) Choi, S. U. S.; Eastman, J. A. *Enhancing Thermal Conductivity of Fluids with Nanoparticles*; ANL/MSD/CP-84938, CONF-951135-29; Argonne National Laboratory: Argonne, IL, 1995. https://www.osti.gov/biblio/196525 (accessed 2022-05-12).
(30) Buongiorno, J. Convective Transport in Nanofluids. *J. Heat Transfer* **2006**, *128* (3), 240−250.
(31) Hayat, T.; Qayyum, S.; Alsaedi, A.; Asghar, S. Radiation Effects on the Mixed Convection Flow Induced by an Inclined Stretching Cylinder with Non-Uniform Heat Source/Sink. *PLoS One* **2017**, *12* (4), e0175584.
(32) Farooq, M.; Khan, M. I.; Waqas, M.; Hayat, T.; Alsaedi, A.; Khan, M. I. MHD Stagnation Point Flow of Viscoelastic Nanofluid with Non-Linear Radiation Effects. *J. Mol. Liq.* **2016**, *221*, 1097−1103.
(33) Basha, H. T.; Sivaraj, R.; Reddy, A. S.; Chamkha, A. J.; Baskonus, H. M. A Numerical Study of the Ferromagnetic Flow of Carreau Nanofluid over a Wedge, Plate and Stagnation Point with a Magnetic Dipole. *AIMS Math.* **2020**, *5* (5), 4197−4219.
(34) Mebarek-Oudina, F. Numerical Modeling of the Hydrodynamic Stability in Vertical annulus with Heat Source of different Lengths. *Eng. Sci. Technol.* **2017**, *20* (4), 1324−1333.
(35) Chabani, I.; Mebarek-Oudina, F.; Vaidya, H.; Ismail, A. I. Numerical Analysis of Magnetic Hybrid Nano-fluid Natural Convective Flow in an adjusted Porous Trapezoidal Enclosure. *J. Mag. Mag. Mater.* **2022**, *564* (2), 170142.
(36) Shafiq, A.; Mebarek-Oudina, F.; Sindhu, T. N.; Rassoul, G. Sensitivity analysis for Walters' B nanoliquid flow over a radiative Riga surface by RSM. *Scientia Iranica* **2022**, *29* (3), 1236−1249.
(37) Raza, J.; Mebarek-Oudina, F.; Lund, L. A. The flow of magnetised convective Casson liquid via a porous channel with shrinking and stationary walls. *Pram. J. Phys.* **2022**, *96*, 229.
(38) Reddy, Y. D.; Mebarek-Oudina, F.; Goud, B. S.; Ismail, A. I. Radiation, Velocity and Thermal Slips Effect Toward MHD Boundary Layer Flow Through Heat and Mass Transport of Williamson Nanofluid with Porous Medium. *Arab. J. Sci. Eng.* **2022**, *47* (12), 16355−16369.
(39) Swain, K.; Mebarek-Oudina, F.; Abo-Dahab, S. M. Influence of MWCNT/Fe_3O_4 Hybrid-Nanoparticles on an Exponentially Porous Shrinking Sheet with Chemical Reaction and Slip Boundary Conditions. *J. Therm. Anal. Calor.* **2022**, *147*, 1561−1570.
(40) Asghar, Z.; Saif, R. S.; Ghaffari, A. Z. Numerical Study of Boundary Stresses on Jeffery-Hamel Flow Subject to Soret/Dufour Effects. *Proc. Inst. Mech. Eng. Part C* **2022**, 095440622211266.
(41) Garimella, S. M.; Anand, M.; Rajagopal, K. R. Jeffery−Hamel Flow of a Shear-Thinning Fluid That Mimics the Response of Viscoplastic Materials. *Int. J. Non-Linear Mech.* **2022**, *144*, 104084.
(42) Hashim; Rehman, S.; Mohamed Tag Eldin, E.; Bafakeeh, O. T.; Guedri, K. Coupled Energy and Mass Transport for Non-Newtonian Nanofluid Flow through Non-Parallel Vertical Enclosure. *Ain Shams Eng. J.* **2022**, 102023.
(43) Khan, S. A.; Hayat, T.; Alsaedi, A. Simultaneous Features of Soret and Dufour in Entropy Optimized Flow of Reiner-Rivlin Fluid Considering Thermal Radiation. *Int. Commun. Heat Mass Transfer* **2022**, *137*, 106297.
(44) Hassan, M.; Mebarek-Oudina, F.; Faisal, A.; Ghafar, A.; Ismail, A. I. Thermal Energy and Mass Transport of Shear Thinning Fluid under Effects of Low to High Shear Rate Viscosity. *Int. J. Thermofluids* **2022**, *15*, 100176.
(45) Hayat, T.; Khan, S. A.; Momani, S. Finite Difference Analysis for Entropy Optimized Flow of Casson Fluid with Thermo Diffusion and Diffusion-Thermo Effects. *Int. J. Hydrog. Energy* **2022**, *47* (12), 8048−8059.
(46) Upadhya, S. M.; Raju, S. V. S. R.; Raju, C. S. K.; Shah, N. A.; Chung, J. D. Importance of Entropy Generation on Casson, Micropolar and Hybrid Magneto-Nanofluids in a Suspension of Cross Diffusion. *Chin. J. Phys.* **2022**, *77*, 1080−1101.
(47) Khan, U.; Ahmed, N.; Mohyud-Din, S. T. Thermo-Diffusion, Diffusion-Thermo and Chemical Reaction Effects on MHD Flow of Viscous Fluid in Divergent and Convergent Channels. *Chem. Eng. Sci.* **2016**, *141*, 17−27.
(48) Al-Saif, A.-S. J. A.; Jasim, A. M. New Analytical Study of the Effects Thermo-Diffusion, Diffusion-Thermo and Chemical Reaction of Viscous Fluid on Magneto Hydrodynamics Flow in Divergent and Convergent Channels. *Appl. Math.* **2019**, *10* (4), 268−300.
(49) Nagler, J. Jeffery-Hamel Flow of Non-Newtonian Fluid with Nonlinear Viscosity and Wall Friction. *Appl. Math. Mech.* **2017**, *38* (6), 815−830.
(50) Rehman, S.; Hashim; Alqahtani, S.; Alshehery, S. Modeling a Non-Newtonian Nanofluid Flow between Intersecting Planes with Slip Mechanism. *Contin. Mech. Thermodyn.* **2023**, *35*, 61.
(51) Keller, H. B. A New Difference Scheme for Parabolic Problems. In *Numerical Solution of Partial Differential Equations-II*; Hubbard, B.,, Ed.; Academic Press, 1971; pp 327−350. DOI: 10.1016/B978-0-12-358502-8.50014-1.
(52) Moradi, A.; Alsaedi, A.; Hayat, T. Investigation of Nanoparticles Effect on the Jeffery−Hamel Flow. *Arab. J. Sci. Eng.* **2013**, *38* (10), 2845−2853.

https://doi.org/10.1021/acsomega.2c05937
ACS Omega 2023, 8, 9121−9136